Short activation domains control chromatin association of transcription factors

Vinson B. Fan[1], Abrar A. Abidi[1], Thomas G.W. Graham[1,2], Xavier Darzacq[1], Max V. Staller[1, 3,4]

[1] Department of Molecular and Cell Biology, University of California Berkeley, Berkeley, CA 94720

[2] Thomas C. Jenkins Department of Biophysics, Johns Hopkins University, Baltimore, MD 21218

[3] Center for Computational Biology, University of California, Berkeley, Berkeley, CA 94720

[4] Chan Zuckerberg Biohub–San Francisco, San Francisco, CA 94158

Abstract

Transcription factors regulate gene expression with DNA-binding domains (DBDs) and activation domains. Despite mounting evidence to the contrary, it is frequently assumed that DBDs are solely responsible for interacting with DNA and chromatin. Here, we used single-molecule tracking of transcription factors in living cells to show that short activation domains can control the fraction of molecules bound to chromatin. Stronger activation domains have higher bound fractions and longer residence times on chromatin. Furthermore, mutations that increase activation domain strength also increase chromatin binding. This trend was consistent in four different activation domains and their mutants. This effect further held for activation domains appended to three different structural classes of DBDs. Stronger activation domains with high chromatin-bound fractions also exhibited increased binding to the p300 coactivator in proximity-assisted photoactivation experiments. Taken together, these results suggest that activation domains play a major role in tethering transcription factors to chromatin, challenging the traditional view that the DBD is the sole driver of genome binding.

Introduction

Transcription factors (TFs) contain DNA-binding domains (DBDs) that bind cognate DNA motifs and effector domains that regulate transcription (Brent and Ptashne, 1985; Keegan et al., 1986; Ptashne, 1988; Struhl, 1989, 1987). DBDs are ordered, conserved, and readily predicted from protein sequences (El-Gebali et al., 2019; Finn et al., 2016). Decades of biochemistry have shown that DBDs are sufficient to bind cognate DNA motifs *in vitro* (Riley et al., 2014; Stormo, 2013). As a result, for most human TFs, only the DBD was used to define the position weight matrices that describe DNA binding specificity (Badis et al., 06 2009; Hume et al., 2015; Jolma et al., 2013; Latchman, 2008; Noyes et al., 2008). Outside the DBD, TFs are predominantly composed of long intrinsically disordered regions (IDRs) that contain short repression domains, which bind corepressor complexes, and activation domains, which bind coactivators (Hahn and Young, 2011; Liu et al., 06 2006; Már et al., 2023; Soto et al., 2021). Activation domain function is separable from DBD function, as demonstrated by cut-and-paste experiments where activation domains retained function when attached to multiple DBDs (Hope et al., 1988; Hope and Struhl, 1986; Ma and Ptashne, 10 1987; Sadowski et al., 10 1988; Sigler, 05 1988; Struhl, 1993, 1987).

In a landmark 1988 review, Ptashne took the evidence supporting TF separability and argued that TFs are modular proteins with independently-acting DBDs and activation domains (Ptashne, 1988). This idea of TF modularity was further cemented when Ptashne and Gann proposed the recruitment model of transcriptional regulation—a TF first binds a cognate DNA motif through its DBD, then recruits transcriptional machinery from solution via its activation domain (Ptashne and Gann, 04 1997). In this view, the activation domains do not contribute to genomic localization, DNA binding, or chromatin binding. There is direct support for the recruitment model *in vitro* (Jeon et al., 2025; Zhou et al., 2024) and indirect support *in vivo* (Crocker et al., 2015; Kawasaki and Fukaya, 2023; Zhang et al., 09 2016). The combination of TF modularity and the recruitment model has led to the widespread textbook model that the DBD is solely responsible for binding the genome (Alberts et al., 2002; Craig et al., 2021; Latchman, 2008). TF modularity has justified genomics programs to measure protein-DNA interactions for isolated DBDs (Badis et al., 06 2009; Barrera et al., 2016; Jolma et al., 2013; Noyes et al., 2008; Zhu et al., 2017). This textbook model predicts that two TFs with the same DBD and different activation domains will have indistinguishable DNA binding and chromatin binding profiles.

Although TF modularity remains a useful first-order approximation of TF function, experts have long recognized the limits of modularity. Careful authors went to length to never use the term modular in review articles (Dubnau and Struhl, 1996; Struhl, 1993, 1989, 1987). From the beginning, some cut-and-paste experiments interfered with DNA binding (Golemis and Brent, 1992). Some short synthetic peptides only work as activation domains when attached to one specific DBD (Lum et al., 2006; Lu et al., 2005). *In vitro*, interactions between activation domains and DBDs can increase DNA binding specificity (Krois et al., 2018; Liu et al., 2008; Ning et al., 2022; Sun et al., 2021). IDRs can increase non-specific binding (Baughman et al., 2022), regulate DNA binding via post-translational modifications (Pufall et al., 2005), or allosterically regulate DNA binding (Li et al., 10 2017). There is long-standing evidence that the DBD does not confer all genomic targeting information because in ChIP-seq experiments, 30-70% of peaks lack a motif for the query TF (Harrison et al., 2011; Jana et al., 2021; Kvon et al., 2012; Spitz and Furlong, 2012; Teytelman et al., 2013). There is also low agreement between the promoters a TF binds and the genes it regulates (Mahendrawada et al., 2025). Finally, there is extensive literature demonstrating how long IDRs—and not DBDs—control TF genomic localization (Brodsky et al., 2020; Gera et al., 2022; Hurieva et al., 2024; Jonas et al., 2023; Kumar et al., 2023; Mindel et al., 2024a, 2024b). These authors show that long IDRs are necessary and sufficient to localize TFs to target promoter genes. Minimal activation domains were reported not to contribute (Brodsky et al., 2020). Although the original data could not distinguish between direct DNA binding and chromatin binding via protein-protein interactions with DNA-bound factors (reviewed in (Staller, 2022)), recent studies suggest an IDR can bind DNA directly (Strugo et al., 2025). This genomic targeting by IDRs has also been seen in human cells (Goldman et al., 2023). These findings can explain why removing the DBD can increase the number of genomic binding sites detected by ChIP-seq (Chen et al., 2014), have little effect on genome binding (Cowling and Cole, 2007), or complement null mutants (Copeland et al., 1996). We have shown that long IDRs control the fraction of TF molecules bound to chromatin for factors in the HIF family (Chen et al., 2022). Other single-molecule imaging studies reported that IDRs impact nuclear diffusion but not genome binding (Callegari et al., 01 2019; Mazzocca et al., 2023). A single-molecule footprinting assay found that a strong activation domain can increase TF occupancy (Doughty et al., 2024). Together, these studies demonstrate how long IDRs or activation domains modulate or override functions ascribed to the DBD.

In this study, we asked whether short activation domains within an IDR are sufficient to control chromatin association. For this work, it is important to distinguish between a TF binding to DNA and a TF binding to chromatin. DNA binding results from direct protein-DNA interaction, is well established for DBDs *in vitro,* and is measured *in vivo* with single-molecule footprinting (Doughty et al., 2024; Stormo, 2013). Chromatin binding includes DNA binding but can also result from protein-protein interactions with histones, other TFs, corepressors, or coactivators that can indirectly tether a TF to DNA (Spitz and Furlong, 2012). Nearly all cell-based assays of TF genome localization (e.g. ChIP-seq or CUT&RUN) measure the combination of DNA binding and chromatin binding.

Here we investigate whether minimal activation domains contribute to chromatin binding. Activation domains recruit remodelers, like BAF, which move nucleosomes (Kadoch and Crabtree, 2015), coactivators, like p300/CBP, which modify chromatin (DelRosso et al., 2024; Dyson and Wright, 2016), and general transcription components like the Mediator complex (Currie et al., 2017; Henley et al., 2020; Lauberth et al., 02 2013; Malik and Roeder, 2010; Tang et al., 07 2013) that recruit RNA polymerase II (Alerasool et al., 2022; Gill et al., 1994). Although mechanistic understanding of activation domains still lags far behind DBDs, recent screens have cataloged many activation domains (DelRosso et al., 2023; Erijman et al., 2020; Morffy et al., 2024; Sanborn et al., 2021) and shown how the strength of acidic activation domains, the oldest and largest class (Sigler, 05 1988), depends on a balance of acidic, aromatic, and leucine residues (DelRosso et al., 2023; Staller et al., 2022, 2018; Udupa et al., 2024). For consistency, we define activation domain strength as the fluorescence of a GFP reporter construct driven by a heterologous promoter.

Using single-molecule tracking (SMT) in live cells, we find that activation domains as short as 39-60 amino acids strongly affect the fraction of synthetic TF molecules bound to chromatin. TFs with a higher bound fraction have increased residence time on chromatin as measured by fluorescence recovery after photobleaching (FRAP). The chromatin-bound fraction and residence time of a series of activation domain mutants correlated with their ability to activate transcription. This effect was observed with activation domains attached to three structurally diverse DBDs, indicating that activation domains can control TF association with chromatin independent of DBD identity. Using pharmacological perturbations and proximity-assisted photoactivation (PAPA) experiments (Graham et al., 2022), we demonstrate this chromatin association results from activation domains binding to coactivator complexes. CUT&RUN experiments revealed all the synthetic TFs bound to

overlapping sets of ATAC-seq accessible loci, suggesting that activation domains are binding to coactivators already engaged with chromatin. These results suggest a key aspect of activation domain function could derive from increasing the ability of a TF to interact with chromatin.

Results

Single-molecule tracking of a synthetic transcription factor

To test whether short activation domains are sufficient to control chromatin binding of TFs, we performed SMT on a synthetic factor. This synthetic TF was developed for high-throughput reporter studies of activation domain function (Staller et al., 2022) and contains an estrogen-binding domain for inducible activation and six synthetic C2H2 zinc fingers (Park et al., 2019) engineered to bind to a DNA motif that is not found in the human genome. To facilitate SMT, we added a HaloTag for labeling with photostable synthetic dyes (Grimm et al., 2021) (Figure 1A, B). At the N-terminus of this synthetic TF, we fused candidate activation domains and their rationally-designed mutants. This synthetic TF is expressed from the weak L40 promoter and has low protein stability (Staller et al., 2022) resulting in low steady-state expression levels. We engineered the cognate reporter into the AAVS1 locus of U2OS cells and derived a monoclonal line to assay transcriptional activity by GFP expression (Figure 1C, Methods). This reporter locus is the only perfect motif match for the synthetic DBD in the genome. We stably integrated each synthetic TF into this cell line and verified that estradiol induction robustly induces GFP expression (Figure 1D).

We performed fast SMT on these synthetic TFs using highly inclined and laminated optical sheet (HILO) illumination at fast (~7.5 ms) frame rates (Figure 1E), localized and tracked single molecules, and a published Bayesian mixture model to infer the distribution of their diffusion coefficients (Heckert et al., 2022). We define proteins with a diffusion coefficient $D < 0.1\ \mu m^2/s$ as immobile and assume immobile molecules are bound to chromatin (Chen et al., 2022; Ferrie et al., 2024). Importantly, this chromatin association does not necessarily indicate direct binding to DNA but could include interactions with factors directly bound to DNA. Molecules with higher diffusion coefficients are untethered and are likely freely diffusing or diffusing in complex with other factors (Ferrie et al., 2022; Staller, 2022). In this work, we focus on the fraction of immobile molecules bound to chromatin.

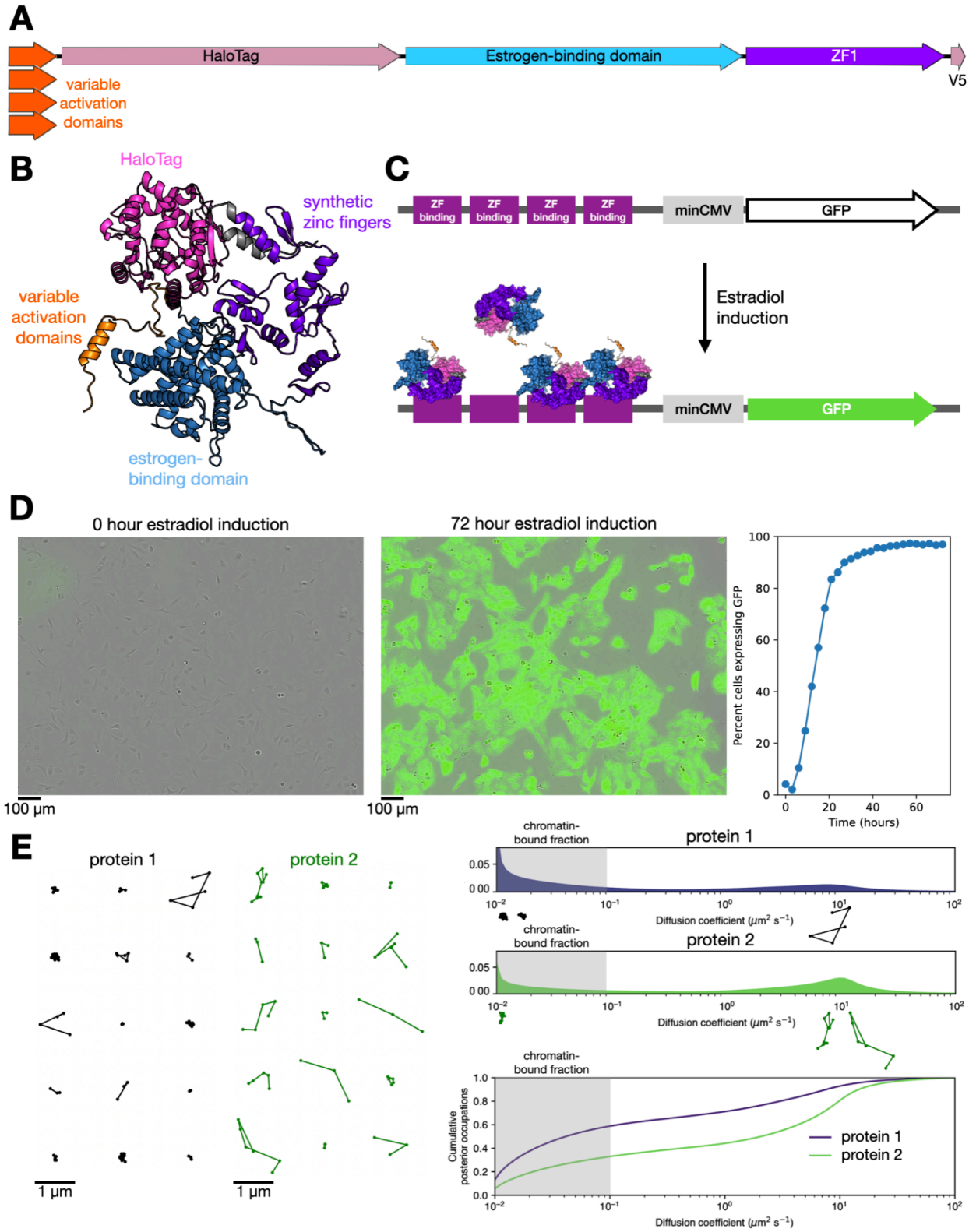
A
HaloTag
Estrogen-binding domain
ZF1
V5
variable
activation
domains
B
HaloTag
synthetic
zinc fingers
variable
activation
domains
estrogen-
binding domain
C
ZF
binding
minCMV
GFP
Estradiol
induction
D
0 hour estradiol induction
72 hour estradiol induction
100 µm
Percent cells expressing GFP
Time (hours)
E
protein 1
protein 2
1 µm
chromatin-
bound fraction
Diffusion coefficient (µm² s⁻¹)
Cumulative
posterior occupations

Figure 1: A synthetic transcription factor for quantifying chromatin association and reporter activity

A: Schematic of the synthetic TF used in this study: activation domains (39-60 amino acids) are fused to HaloTag, an estrogen-binding domain, six synthetic C2H2 zinc fingers (ZF1), and a V5 epitope tag. Black line indicates linkers between domains.

B: AlphaFold2 model of the synthetic TF.

C: Schematic of the synthetic reporter locus (not to scale) installed at AAVS1. Four zinc-finger binding sites are engineered upstream of a minimal promoter, minCMV. These elements are upstream of GFP, which is produced in response to estradiol induction.

D: Overlay of GFP and phase-contrast images of reporter-bearing cells expressing VP16-synthetic transcription factor at 0 hours (left) and 72 hours (right) after estradiol induction. Quantification of the percentage of GFP-positive cells over time from live imaging is shown in the right plot.

E: Left: trajectories extracted from SMT movies from cells expressing two example proteins. Thousands of these trajectories are pooled to generate inferred diffusion spectra, right. Lower panel indicates the cumulative distribution function of the diffusion spectra. We consider the shaded gray region ($D < 0.1$ $\mu m^2/s$) the chromatin-associated fraction of a protein.

Short activation domains control the fraction of TF molecules bound to chromatin

Given the evidence that long IDRs can control the fraction of molecules bound to chromatin, we tested the hypothesis that minimal activation domains can also contribute to this phenotype. In previous examples, the IDRs that controlled the bound fraction were the majority of the protein (Chen et al., 2022). Here, our synthetic TF is ~800 AAs and the activation domain is 39-60 residues on the N-terminus.

Despite comprising only 5-7% of the total polypeptide sequence, these short activation domains dominated the chromatin bound fraction of our synthetic TF. Three acidic activation domains derived from VP16, CITED2, and HIF1α each yielded different bound fractions and diffusion spectra (Figure 2A). These differences were also apparent in jump-length histograms and generally agreed with parameters modeled from Spot-On (Hansen et al., 2018) (Figure 2—figure supplement 1), independently validating this result. This bound fraction was positively correlated with GFP expression of the reporter locus measured by flow cytometry (Figure 2B, C), suggesting a link between the strength of activation domains and their propensity to associate with chromatin (Figure 2D). The synthetic TF without an activation domain (hereafter the empty TF) also had a low (but not the lowest) fraction of molecules bound to chromatin.

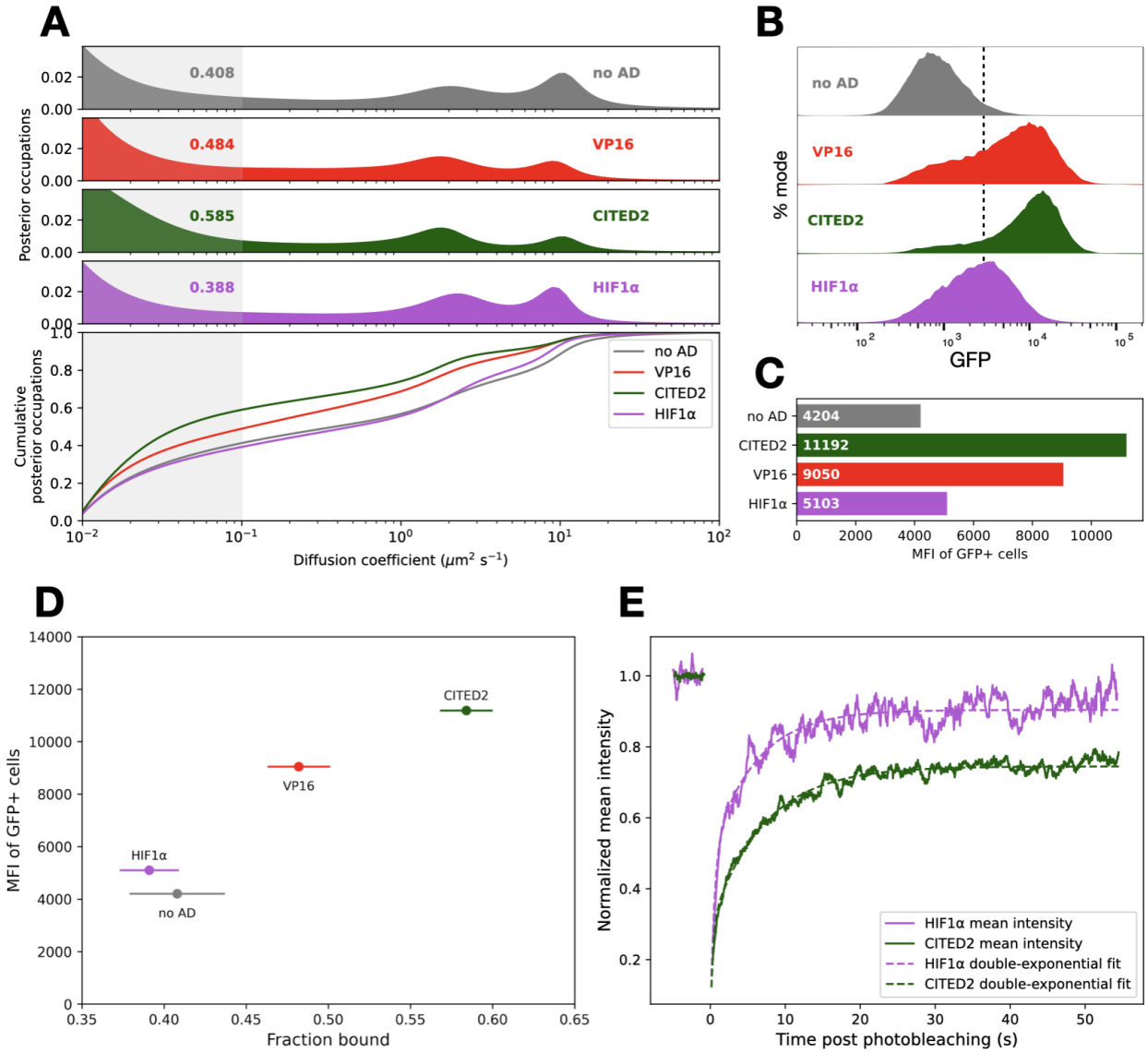

Figure 2: Short activation domains are sufficient to control the fraction of TF molecules bound to chromatin

A: Diffusion spectra (top) and cumulative distributions (bottom) of synthetic TFs bearing various activation domains. Numbers indicate the fraction of molecules with diffusion coefficients below 0.1 $\mu m^2/s$ (shaded region), which we infer to be chromatin-bound.

B: Flow cytometry measurements of cells bearing various activation domains after 24 hours of estradiol treatment. Distributions are shown in the top panel, where the dashed line is an arbitrary gate for GFP-positive cells.

C: Barplot for mean fluorescence intensity (MFI), the geometric mean of GFP values for cells in the positive gate.

D: For each synthetic TF, the MFI of GFP+ cells is plotted against its bound fraction. Error bars indicate bootstrapping standard deviations of the bound fraction (Methods).

E: HIF1α and CITED2 FRAP recoveries over time plotted as rolling means (solid lines). Curve fits to a double-exponential equation (Methods) are shown in dashed lines.

As previously reported (Driouchi et al., 2025; Walther et al., 2024), we find substantial cell-to-cell variability when making SMT measurements in these cell lines (Figure 2—figure supplement 2), which necessitated large datasets with many cells and trajectories for reporting reproducible diffusion spectra (Methods; Supplementary Table 2). The difference in bound fractions also held when these synthetic TFs were transfected into cells without reporter loci (Figure 2—figure supplement 3), implying that the majority of immobile molecules bound nonspecifically to genomic sites without a match to the cognate motif.

SMT at fast frame rates provides snapshots of the diffusive states of these factors but cannot accurately determine how long a given factor remains bound. To complement this experiment, we measured TF residence time on chromatin with fluorescence recovery after photobleaching (FRAP, Figure 2E, Figure 2—figure supplement 4). We fit our FRAP recovery curves to a double-exponential equation (Methods, Supplementary Table 1, (Mueller et al., 2012). We found that the SMT bound fraction correlated with FRAP recovery times, with stronger activation domains conferring longer dwell times. This recovery time difference is consistent with another synthetic system where strong activation domains have longer dwell time on chromatin (Trojanowski et al., 2022). Together, these results indicate that stronger activation domains have a higher fraction of molecules bound to chromatin and that these molecules have longer residence times on chromatin.

Mutations in activation domains modulate chromatin binding

Intrigued by the apparent correlation between activation domain strength and bound fraction, we investigated multiple allelic series of mutations that increased and decreased activity of our activation domains (Staller et al., 2022). We selected mutants that we have previously shown to have large effects on reporter gene activity and that change 1-7 residues in each activation domain.

Within each allelic series, we saw a positive correlation between activation domain strength and bound fraction. Stronger activation domain mutants had higher bound fractions. These mutations change activity by perturbing different physicochemical parameters. For CITED2 (Figure 3A), two alleles that decrease activity, either by mutating key hydrophobic residues (motif mutation) or replacing all six leucines with phenylalanines (L>F), decreased bound fraction. A CITED2 allele that neutralizes a single positive charge (K>A) increased activity and increased bound

fraction. For VP16, two alleles that abrogate activation domain activity, F442A (Cress and Triezenberg, 01 1991) and 7As, both reduced the bound fraction (Figure 3B). In HIF1α, adding acidity by mutating three arginines to aspartates (R>D) or two glutamines and one asparagine to glutamate (QN>E) increased the fraction bound (Figure 3C). In the SREBP activation domain, removing aromatic and/or leucine residues decreased activity and decreased the bound fraction (Figure 3—figure supplement 1). We employed a bootstrapping approach to estimate error in SMT diffusion spectra (Methods, Figure 3—figure supplement 2) and noted that this trend held within each allelic series and across the full set of mutants (Figure 3D). In individual cells, the bound fraction was not correlated with TF abundance (Figure 3—figure supplement 3) or the charge of the activation domain (Figure 3—figure supplement 4). Within each allelic series, stronger activation domain mutants had higher bound fractions, and weaker mutants had lower bound fractions.

Furthermore, for HIF1α, the QN>E allele had slower FRAP recovery, indicating a longer residence time on chromatin (Figure 3—figure supplement 5D). These data support the idea that strong activation domains increase the fraction of TF molecules bound to chromatin and extend the duration of their binding.

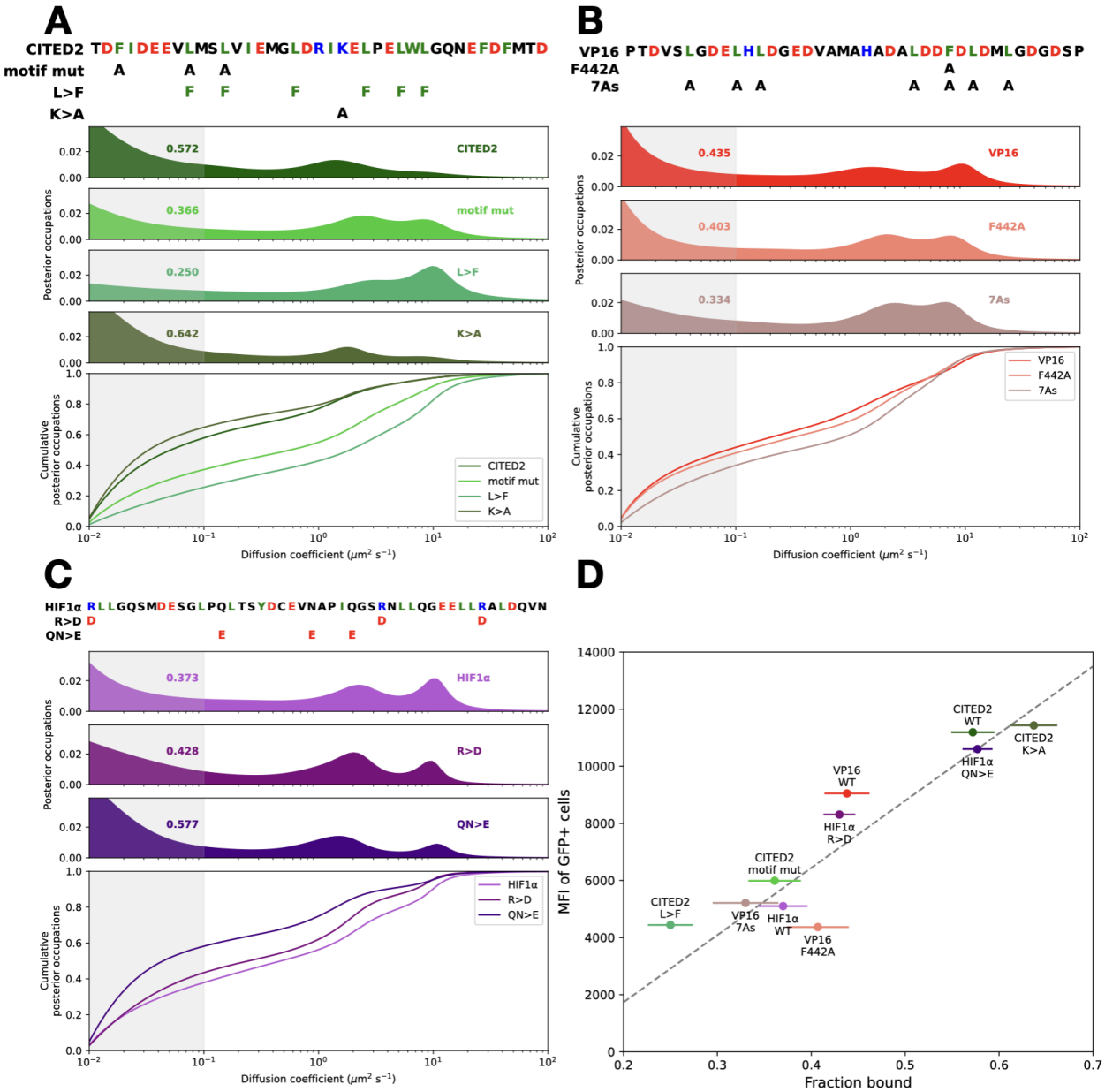

Figure 3: Mutations in individual activation domains modulate the fraction of molecules bound to chromatin

A: The amino-acid sequence of CITED2 and its mutant constructs is shown above their diffusion spectra and the cumulative distributions. Numbers indicate the fractions bound, the probability density in the shaded region of the diffusion spectra.

B: as in A for VP16.

C: as in A for HIF1α.

D: Summary of activation domain activity and chromatin-bound fractions. Mean fluorescence intensity of GFP+ cells plotted against bound fractions. Error bars indicate standard deviations of a cell-wise bootstrapping scheme (Methods, Figure 3—figure supplement 2).

Activation domains control chromatin binding of a second DBD

We next tested whether the observed relationship between activation domain strength and bound fraction depends on the DBD of our synthetic TF. We replaced the synthetic zinc fingers with the SOX2 DBD, which belongs to a different structural family, the high-mobility group (HMG) DBDs (Figure 4A). These domains are minor-groove binders with many specific cognate sites throughout the genome. For this orthogonal DBD, our CITED2-K>A mutant had a dramatically higher fraction bound than WT, while the inactive motif mutant modestly decreased chromatin association (Figure 4A). The L>F mutation in this chimeric factor prevented its localization to the nucleus, precluding SMT. None of these constructs activated our GFP reporter (Figure 4—figure supplement 1). This last finding further reinforces that most of the observed chromatin binding in SMT is not at the reporter locus. With this second DBD, strong activation domains show more chromatin binding.

Activation domains control chromatin binding of full-length TFs

We next investigated activation domain mutations in full-length TFs. We previously showed that the bound fraction of the HIF1α and HIF2α paralogs are controlled by long IDRs, not their DBDs (Chen et al., 2022). In chimeric TFs, the IDR of HIF2α yields more chromatin binding than that of HIF1α. Previous studies were conducted in VHL-deficient renal carcinoma cells, which resulted in the stabilization of HIF proteins in this cell line (Brodaczewska et al., 2016). We recapitulated these results in our U2OS cells using deferoxamine, a drug that prevents HIF degradation and mimics aspects of hypoxia (Guo et al., 2006). In this condition, we reproduced the effect of IDR swaps on the diffusion of HIF factors: HIF2α had a higher bound fraction than HIF1α, and the HIF2α IDR was sufficient to confer this higher bound fraction (Figure 4B). Conversely, the HIF1α IDR conferred a lower bound fraction when attached to the HIF2α DBD. For these paralogs, the IDR controls the bound fraction.

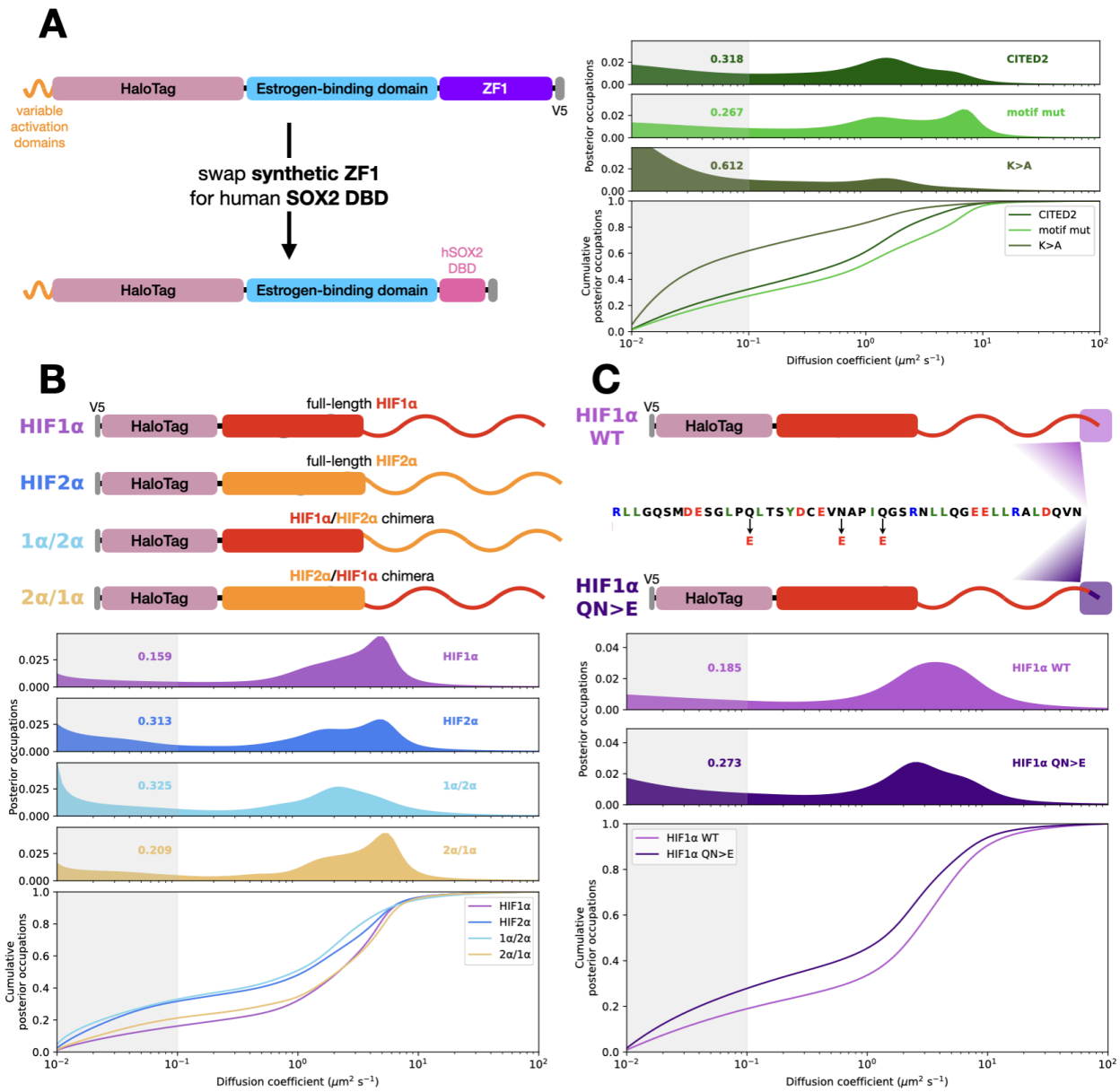

Figure 4: Activation domain alleles control the fraction of molecules bound to chromatin when fused to an alternative DBD or in a full-length TF

A: Left: We replaced the synthetic zinc finger DBD with the human SOX2 DBD. Right: Diffusion spectra and cumulative distributions for three alleles of CITED2. Shaded region indicates density contributing to the bound fraction.

B: Top: Schematic of the HIF1α and HIF2α IDR swap chimeras from (Chen et al., 2022). Bottom: Diffusion spectra and cumulative distributions of the constructs shown. The HIF1α IDRs control the fraction of molecules bound to chromatin under hypoxic conditions.

C: Top: We introduced three superactivating point mutations (QN>E) into full-length HIF1α's second activation domain. Bottom: Diffusion spectra and cumulative distributions of the constructs shown. These three mutations HIF1α increase the fraction of molecules bound to chromatin, recapitulating the differences seen in synthetic TFs.

We tested if the mutations in the activation domain could control the fraction of full-length HIF1α bound to chromatin. Introducing the strongest of these mutations, QN>E, into AD2 (C-terminal activation domain) of full-length HIF1α increased the fraction of molecules bound to chromatin (Figure 4C). This result shows that the strength of minimal activation domains in endogenous factors can control the fraction of molecules bound to chromatin. Further, this experiment demonstrated that the relationship between activation domain strength and bound fraction holds for another structurally distinct DBD, the basic helix-loop-helix (bHLH) family.

Together, we found that strong activation domains control the bound fraction of one synthetic and two natural DBDs. These DBDs are taken from three structurally distinct classes: zinc finger, HMG, and bHLH. We have further shown this result holds for both synthetic TFs and full-length endogenous TFs. We speculate that acidic activation domains may contribute to the fraction of molecules bound to chromatin for other full-length TFs.

Quantifying activation domain coactivator interactions *in vivo*

We tested the hypothesis that protein-protein interactions between activation domains and coactivators can explain the positive correlation between activation domain strength and the fraction of molecules bound to chromatin. If increasing activation domain binding to known coactivator partners can increase TF chromatin binding, it would explain our results without invoking any new molecular mechanisms. *In vitro*, strong activation domains bind coactivators more tightly than weak ones (DelRosso et al., 2024; Henderson et al., 09 2018; Sanborn et al., 2021). In the nucleus, coactivators are limiting for transcriptional activity (Gillespie et al., 2020) and have long residence times on chromatin (Cho et al., 07 2018; Sanborn et al., 2021). For p300, the majority of molecules are bound to chromatin at steady state (Ferrie et al., 2024).

To assess more directly whether chromatin binding of synthetic TFs correlates with coactivator binding, we used proximity-assisted photoactivation (PAPA), in which excitation of a "sender" fluorophore reactivates a nearby "receiver" fluorophore from a dark state, thereby revealing proximity between two labeled proteins (Figure 5A). To this end, we expressed different SNAP-tag2-tagged (Kühn et al., 2025) synthetic TFs in a U2OS cell line with Halo-tagged endogenous p300 (Ferrie et al., 2024). After labeling SNAP-tag with the receiver fluorophore JFX650 and HaloTag-p300 with the sender fluorophore JF549, we placed JFX650 in a dark state with 639 nm illumination and

assayed proximity dependent reactivation following excitation of JF549 with 561 nm light. As previously described, we used direct reactivation of JFX650 with 405 nm light as an internal normalization standard (Dahal et al., 2025; Graham et al., 2025, 2022) and calculated a normalized PAPA ratio relative to nuclear SNAP-tag alone, a non-interacting negative control (Abidi et al., 2025) (Methods, Figure 5—figure supplement 1). A very marginal PAPA signal was observed between p300 and the synthetic TF without an activation domain, while a small but significant increase was observed upon fusion to the HIF1α activation domain (Figure 5B). A dramatic increase in PAPA signal was observed for the superactive mutants, consistent with stronger binding to p300. These data support the model that activation domains increase chromatin binding of TFs by engaging coactivators. These results also demonstrate that PAPA can detect interactions between a coactivator and minimal activation domains and that this measure is commensurate with activation domain strength.

In addition, we can examine the diffusion spectra of the p300 proximal molecules (green-reactivated) and the total population (violet-reactivated). For the two superactive mutants, this analysis shows that the p300 proximal population has a much higher bound fraction (Figure 5D-E). Increased binding between synthetic TFs and p300 measured by PAPA correlated with a higher chromatin bound fraction in the SMT. Together, these results support the idea that activation domain coactivator binding can tether TFs to chromatin.

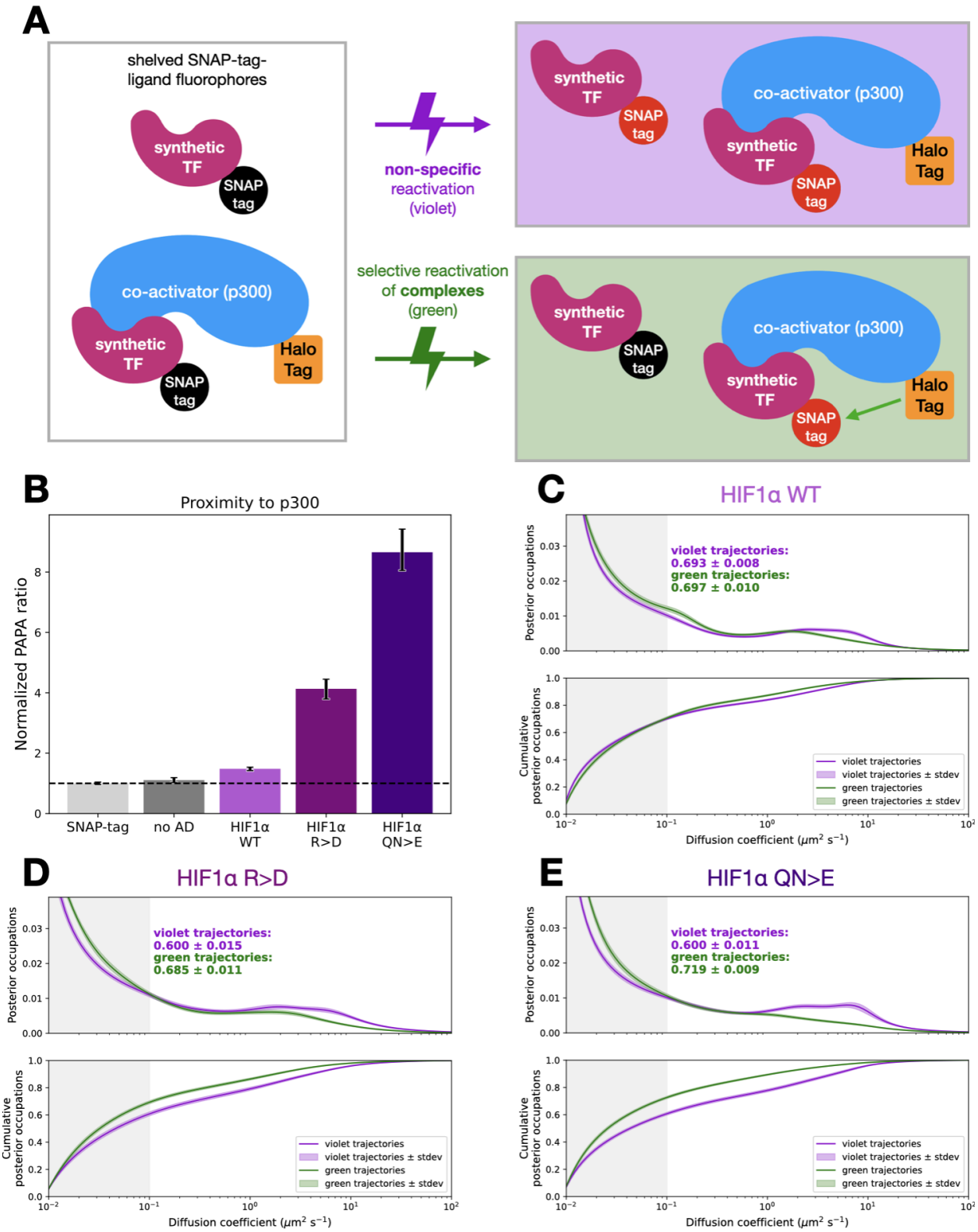
A
shelved SNAP-tag-ligand fluorophores
synthetic TF
SNAP tag
co-activator (p300)
Halo Tag
non-specific reactivation (violet)
selective reactivation of complexes (green)
B
Proximity to p300
Normalized PAPA ratio
SNAP-tag
no AD
HIF1α WT
HIF1α R>D
HIF1α QN>E
C
HIF1α WT
violet trajectories: 0.693 ± 0.008
green trajectories: 0.697 ± 0.010
D
HIF1α R>D
violet trajectories: 0.600 ± 0.015
green trajectories: 0.685 ± 0.011
E
HIF1α QN>E
violet trajectories: 0.600 ± 0.011
green trajectories: 0.719 ± 0.009
Posterior occupations
Cumulative posterior occupations
Diffusion coefficient (μm² s⁻¹)
violet trajectories
violet trajectories ± stdev
green trajectories
green trajectories ± stdev

Figure 5: Proximity-assisted photoactivation (PAPA) of synthetic TFs show that stronger activation domains promote interaction with p300
A: Schematic of our PAPA experiment using p300 endogenously tagged with HaloTag and an exogenous SNAP-tagged synthetic TF. First, red SNAP-tag-liganded dyes are shelved (left, Methods). A pulse of violet light (405 nm) indiscriminately reactivates these shelved dyes, while green light (561 nm) excites the sender, HaloTag-liganded dye, which reactivates nearby SNAP-tag dyes selectively.
B: Normalized PAPA ratio quantifying the proximity between p300-HaloTag and the constructs labeled. Error bars are 95% confidence intervals derived by bootstrapping (Methods).
C: Diffusion spectra and cumulative distributions after segregation of green-reactivated (p300 proximal molecules) and violet-reactivated (direct reactivation) trajectories for cells expressing HIF1α WT. Density in the gray shaded region is quantified as the bound fraction. Light green and purple shading denotes the standard deviation of bootstrapping trials.
D: as in (C) for HIF1α RK>D.
E: as in (C) for HIF1α QN>E.

Disrupting coactivator function perturbs TF-chromatin associations

We further investigated if activation domain binding to coactivators can tether TFs to chromatin by pharmacologically perturbing coactivator function. First, we used norstictic acid to selectively disrupt VP16 binding to the Med25 domain of Mediator (Garlick et al., 2021). Like most coactivators, Mediator has a longer dwell time on DNA than that of sequence-specific TFs (Cho et al., 07 2018; Whitney and Lionnet, 2024). If the synthetic TF with VP16 is tethered to chromatin via activation domain interactions with Med25, norstictic acid treatment would decrease the fraction of molecules bound to chromatin. In line with this prediction, norstictic acid caused a small but significant decrease in the bound fraction of synthetic TF with VP16 (Figure 6A). The empty TF experienced no significant change in binding (Figure 6B), and two alleles of VP16 also showed decreases in fraction bound in response to norstictic acid (Figure 6—figure supplement 1). This perturbation further supports the idea that synthetic TFs can be tethered to chromatin by activation domain interactions with coactivators.

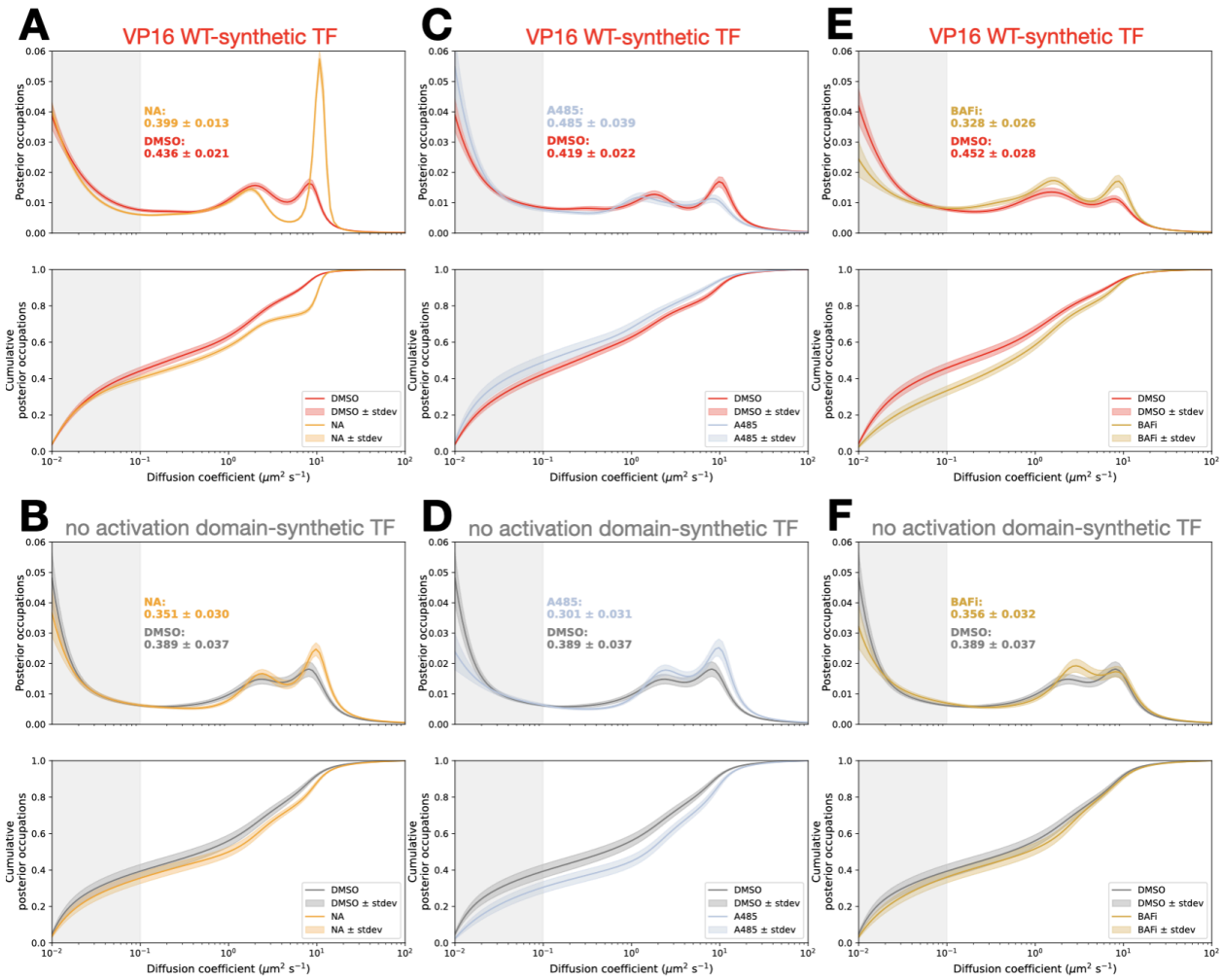

Figure 6: Perturbing coactivator function alters TF bound fraction

A: VP16-synthetic TF diffusion spectra and cumulative distributions for cells treated for two hours with norstictic acid or vehicle (DMSO). Density in light gray is quantified as the bound fraction. Shading around the spectra and cumulative distributions indicates standard deviation of bootstrapping trials.

B: Diffusion spectra and cumulative distributions of cells expressing the synthetic TF with no activation domain treated for two hours with norstictic acid or vehicle (DMSO). Density in light gray is quantified as the bound fraction. Shading around the spectra and cumulative distributions indicates standard deviation of bootstrapping trials.

C: as in (A) for A485, a p300 inhibitor.

D: as in (B) for A485, a p300 inhibitor. The DMSO curve is repeated from (B).

E: as in (A) for BRM-014, a BAF inhibitor (BAFi).

F: as in (B) for BRM-014, a BAF inhibitor (BAFi). The DMSO curve is repeated from (B).

For the second pharmacological perturbation, we selected the coactivator p300, which has a high bound fraction, a relatively long residence time (Ferrie et al., 2024), and is a key binding partner for the HIF1α, CITED2, and VP16 activation domains (Dyson and Wright, 2016). Inhibition of p300 with A485 inhibits catalytic activity, decreases global transcription (Lasko et al., 2017), and increases the fraction of p300 molecules bound to chromatin (Ferrie et al., 2024). Under A485, we predict that the same steady state binding between an activation domain and p300 will result in more synthetic TF molecules binding to p300 on chromatin and give the appearance of more synthetic TF binding to chromatin. Consistent with this prediction, A485 treatment mildly but significantly increased the fraction of synthetic TF with VP16 bound to chromatin relative to control (Figure 6C). The empty synthetic TF experienced the opposite effect, with a decrease in binding to chromatin (Figure 6D). Together, the A485 and norstictic acid perturbations support the idea that TFs can be tethered to chromatin through protein-protein interactions with coactivators.

As a third perturbation of coactivator function, we inhibited the BAF (mammalian Swi/Snf) complex with BAFi (BRM014). BAF inhibition leads to rapid genome-wide chromatin compaction and decreased global transcription (Schick et al., 2021). In single-molecule footprinting experiments, inhibiting BAF decreased promoter occupancy of a Tet-VP48 synthetic TF (Doughty et al., 2024). For our synthetic TF, inhibition of BAF significantly decreased the fraction of molecules bound to chromatin relative to the vehicle control (Figure 6E). The empty synthetic TF did not experience a significant change in binding (Figure 6F). This result suggests that a substantial portion of our immobile TFs are binding chromatin at open or actively-transcribing loci.

Synthetic transcription factors bind active loci genome-wide

The increases in chromatin binding measured by SMT cannot distinguish between stronger binding to the same genomic loci and binding to new genomic loci. To differentiate between these two possibilities, we undertook CUT&RUN experiments (Skene and Henikoff, 2017) on five of our synthetic TFs (Figure 7A). For full-length HIF1α and HIF1β TFs, CUT&RUN experiments indicated most genomic loci are bound by both TFs, implying that an increased bound fraction in SMT experiments is primarily due to higher occupancy at the same loci (Chen et al., 2022). This result sets the expectation that our activation domain mutations that increase chromatin bound fraction in SMT are unlikely to bind new genomic loci and instead will have higher occupancy at the same loci across the genome.

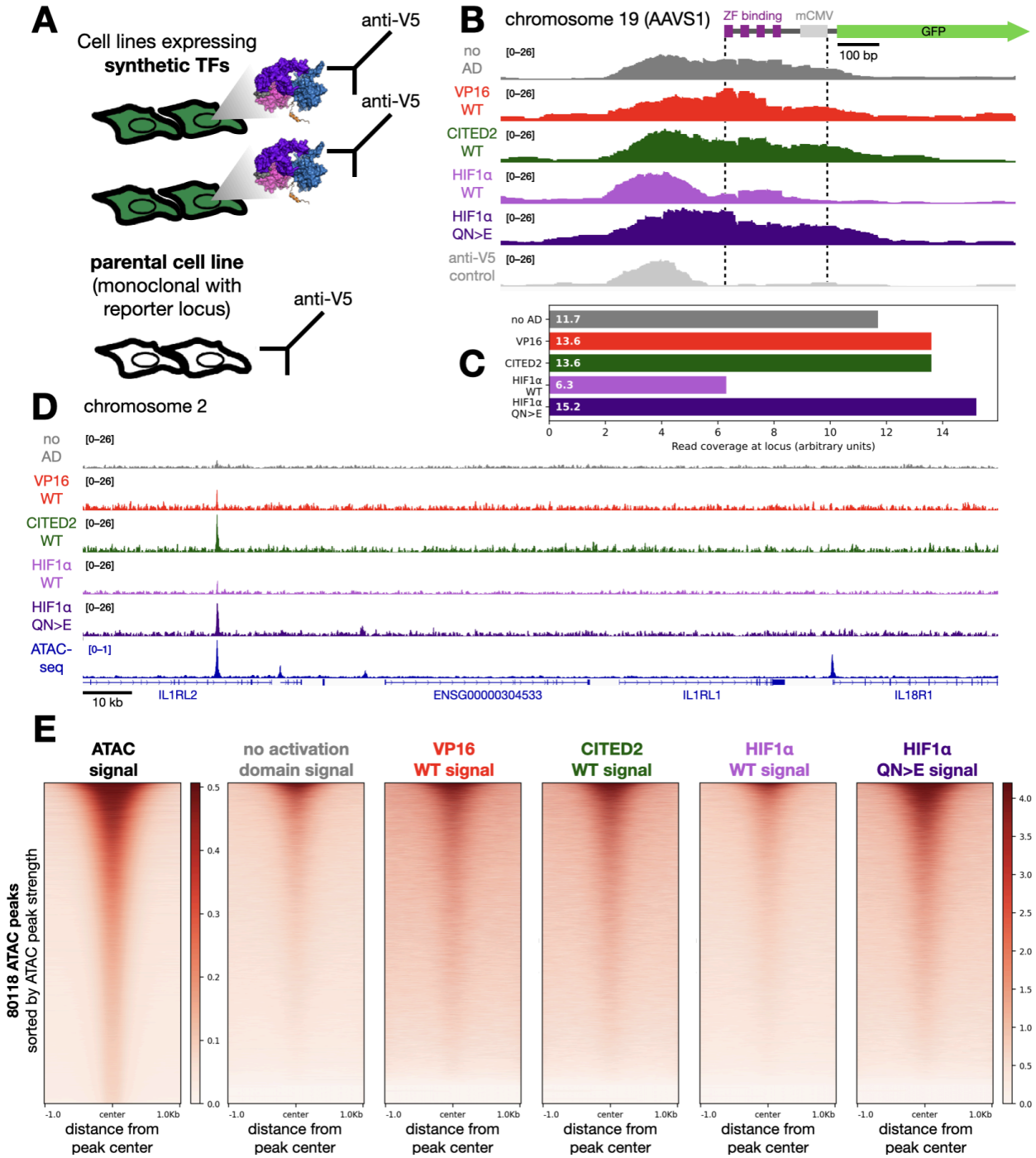

Figure 7: CUT&RUN on synthetic TFs with different activation domains reveals most binding occurs at open chromatin

A: We performed CUT&RUN on the parental cell line bearing the GFP reporter locus and five cell lines, each expressing synthetic TFs with a variable activation domain. Cells for all conditions were probed with an anti-V5 antibody, which should bind specifically only to the V5 epitope of the synthetic TFs.

B: Genomic binding signal at the engineered AAVS1 locus, shown to scale. All the synthetic TFs, including the empty TF, bound the cognate binding sites in the reporter construct.
C: Mean binding signal of the various synthetic TFs between the dashed lines of (B), which include the ZF1 binding sites and minimal promoter.
D: Binding of synthetic TFs and ATAC-seq signal at an exemplary locus. TF binding signal is strongest at ATAC-seq peaks, with stronger activation domains conferring more genomic binding in some cases. Not all ATAC-seq peaks are bound by the synthetic TFs.
E: ATAC-seq (left) and synthetic TF factor binding (right plots) signals plotted across 80118 ATAC-seq peaks, sorted by decreasing ATAC-seq peak strength. The five synthetic TFs share a color scale; the ATAC-seq signal uses a separate scale. Binding patterns for the synthetic TFs generally follow the strength of the ATAC-seq signal.

All the TFs, including the empty TF, were bound to the cognate binding sites of the reporter gene at the AAVS1 locus. Normalizing between samples revealed that the HIF1α QN>E superactive mutant had more occupancy than the WT HIF1α TF (Figure 7C). Genome-wide, the binding profiles of all synthetic TFs mostly overlapped pre-existing ATAC-seq peaks (Figure 7D, Figure 7—figure supplement 1A). The HIF1α superactive allele bound more loci than the WT allele, but the patterns were highly overlapping (Figure 7—figure supplement 1B). Together, these results indicate that most synthetic TF binding events occur at accessible loci. We conclude that the increased bound fraction we observe in the SMT primarily results from more binding to the same active loci.

Discussion

According to the textbook model of TF function, genome binding is controlled solely by the DBD and not influenced by IDRs, much less by short activation domains. We broke this expectation by demonstrating that short activation domains can control the fraction of TF molecules bound to chromatin. Mutations that increase activation domain strength in reporter assays increase the fraction of molecules bound to chromatin. Conversely, mutations that decrease activation domain strength decrease the fraction of molecules bound to chromatin. This trend holds for allelic series of four acidic activation domains, for three structurally diverse DBDs, and for synthetic and full-length TFs. Our result adds to the accumulating cracks in the standard model of TF behavior (Chen et al., 2022; Fallacaro et al., 2024; Goldman et al., 2023; Sun et al., 2021).

SMT has revealed many new dimensions of TF nuclear dynamics and has been instrumental for our discovery. The technique has shown that TF-chromatin

interactions are generally short-lived (Brouwer and Lenstra, 2019; Lionnet and Wu, 2021; Liu et al., 2014), that coactivator chromatin binding is long-lived (Ferrie et al., 2024), and that IDRs can make larger contributions to chromatin binding than DBDs (Chen et al., 2022). Here we add that minimal activation domains can control the fraction of molecules bound to chromatin. Our results are consistent with an SMT study of an activation domain deletion in p53 showing reduced association with dense chromatin (Mazzocca et al., 2023).

There are three hypotheses for how increasing activation domain strength causes a higher fraction of TF molecules bound to chromatin: (1) activation domains could directly bind DNA, (2) activation domains could modulate DBD interactions with DNA, or (3) activation domains could bind to coactivators that are bound to chromatin, tethering the TF to chromatin.

Our short acidic activation domains are unlikely to bind DNA directly due to electrostatic repulsion: both the activation domains and DNA are negatively charged and repel each other. While protein net charge can play a large role in nuclear diffusion (Xiang et al., 2020), we found no correlation between net charge and fractions bound in factors we tested (Figure 3—figure supplement 4).

It is also possible our activation domains are interacting with the DBD to modulate DNA binding, an emerging theme in TF biology (Baughman et al., 2022; Bentley et al., 2023; Bjarnason et al., 2024; He et al., 2019; Krois et al., 2018; Sun et al., 2021). For our results, intramolecular interactions are not the main drivers of chromatin binding because the phenotype is consistent across three structurally distinct DBDs.

Our PAPA experiments support the hypothesis that protein-protein interactions between activation domains and coactivators explain the positive correlation between activation domain strength and the fraction of TF molecules bound to chromatin. The overall chromatin-bound fraction of SNAP-tagged synthetic TFs was higher than that of the Halo-tagged versions, perhaps reflecting differences in physical properties of the two tags such as volume and charge (Figure 3C vs Figure 5C-E violet curves). TFs reactivated by PAPA from p300 had a higher chromatin-bound fraction than those directly reactivated by violet light (DR), indicating the expected correlation between p300 binding and chromatin binding (Figure 5). Compared to WT, the two superactive HIF1α alleles showed stronger binding to p300 by PAPA and a more pronounced shift toward chromatin-bound molecules when comparing PAPA to DR trajectories. Curiously, while the bound fraction of PAPA trajectories increased with activation

domain strength, DR trajectories if anything showed the opposite trend. One possible explanation is that a large fraction of TF molecules bind p300, and each round of PAPA followed by re-bleaching depletes these complexes from subsequent rounds of direct reactivation—with more interaction resulting in greater depletion. This work marks the first time that PAPA has been applied to measure TF-coactivator interactions in vivo, which we anticipate will be a powerful new experimental approach to study transcription. Together with the PAPA experiments, the pharmacological perturbations support our hypothesis that activation domain-coactivator interactions strongly influence TF binding to chromatin (Figure 8).

In the CUT&RUN data, stronger activation domains cause higher occupancy at the reporter locus, but the vast majority of other genomic binding occurs at other active loci. Consequently, we believe our activation domain mediated chromatin binding is distinct from the ability of long IDRs to direct TFs to specific genomic loci (Brodsky et al., 2020; Gera et al., 2022; Goldman et al., 2023; Hurieva et al., 2024; Mindel et al., 2024a). Instead, we believe the SMT is observing the same underlying biological process that causes activation domains to enhance promoter occupancy in single-molecule footprinting experiments (Doughty et al., 2024) and long TF residence times on promoters (Schaepe et al., 2025).

Genome binding is an emergent property of full-length TFs, with contributions from the DBD, activation domains, and their interactions. In textbook models, the DBD binds DNA first, and then the activation domain recruits the coactivators. We speculate that recruitment can occur in both directions: sometimes the first event will be the activation domain binding to a coactivator that is already engaged at an active locus, and then the DBD will bind the local DNA (Figure 8). Different activation domains bind distinct coactivators (Alerasool et al., 2022), but only some of these interactions, which can have affinities of 10 nanomolar (Berlow et al., 2017; De Guzman et al., 2004), will be be strong enough to tether TFs to chromatin.

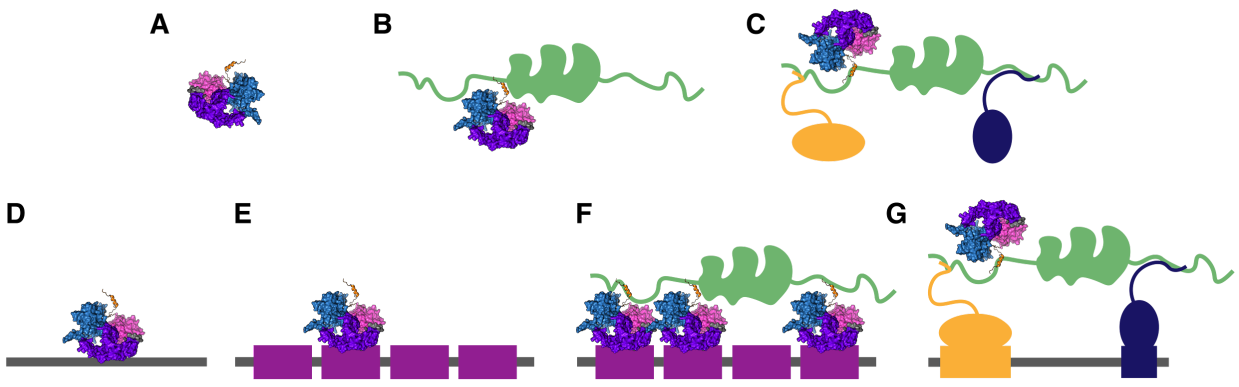

Figure 8: Model for how activation domains contribute to chromatin binding by interactions with coactivators
A: A solitary TF diffusing in the nucleoplasm, a lone wolf.
B: A TF bound to a coactivator with its activation domain diffusing through the nucleoplasm.
C: Three TFs bound simultaneously to a coactivator diffusing in the nucleoplasm as a complex or wolfpack.
D: A TF nonspecifically-bound to random DNA.
E: A TF specifically bound with its DBD to a cognate DNA motif at the reporter locus.
F: TFs specifically bound to motifs at the reporter locus and simultaneously bound to a coactivator.
G: Proposed model for how the activation domain tethers the synthetic TF to chromatin through the coactivator. This situation occurs at active loci where the coactivator has been recruited by the orange and blue TFs.

Our results also challenge the traditional interpretation of activation domain strength. Previously, we had assumed that all our synthetic TFs had similar DNA occupancy because they have the same DBD. Our results here show that strong activation domains increase occupancy at a reporter locus. As a result, the higher reporter activity is a convolution of more binding and more coactivator recruitment. This finding motivates the need for new assays for activation domain function that can separate binding from reporter activity.

In this work, we focused on the fraction of molecules bound to chromatin. We also see some changes in the distribution of inferred diffusion constants of mobile molecules, some of which are bimodal. After norstictic acid treatment, the slow-moving population shrank and the fast-moving population grew. The slow-moving population is also prominent in the PAPA data. We speculate that the slow-moving population might be TFs bound to coactivators exploring the nucleus in clusters or “wolf packs,” (Figure 8C) as we previously hypothesized (Staller, 2022).

Figure supplements

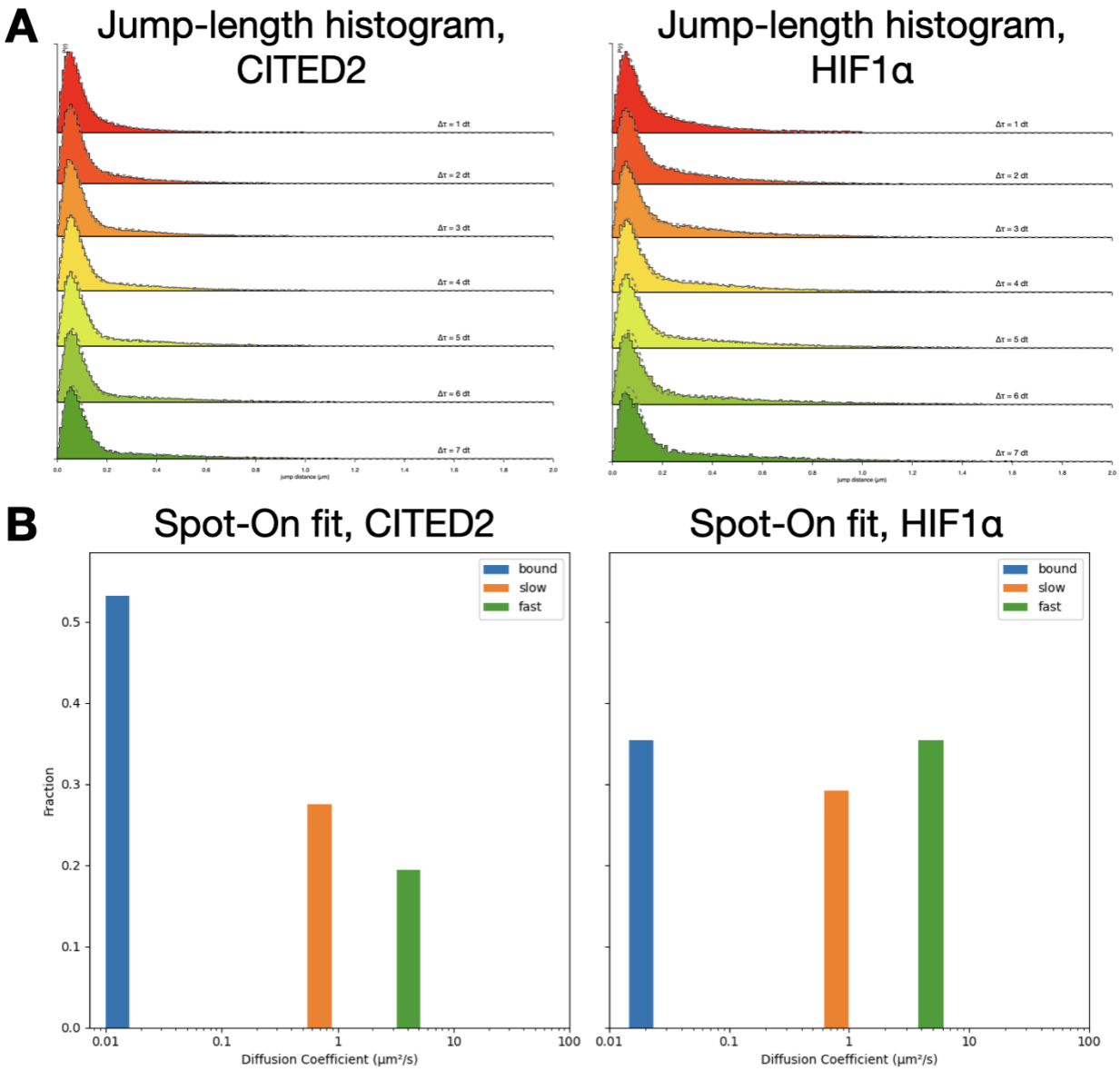

Figure 2—figure supplement 1: Jump length histograms and Spot-On fits for two synthetic transcription factors

A: Jump-length histograms of CITED2-synthetic TF and HIF1α-synthetic TF over increasing frame intervals.
B: Graphical representation of three-state Spot-On fits to the jump-length histograms shown in (A). Height of the bars indicates population fraction, and position along the x-axis denotes the diffusion coefficient of the fit. Both fractions bound and diffusion coefficients are consistent with the analyses shown in the main text.

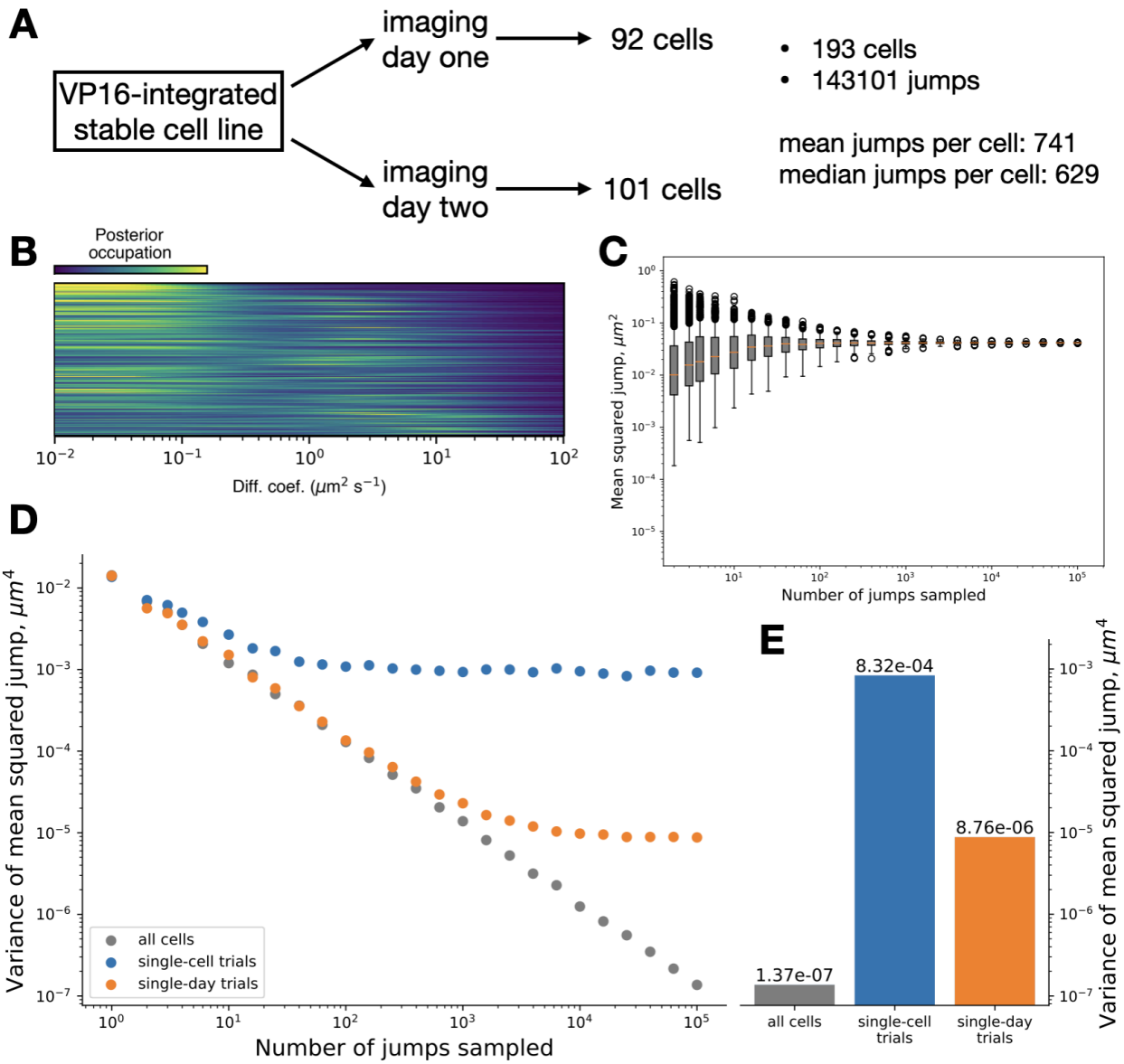

Figure 2—figure supplement 2: Analysis of an SMT dataset for sources of variance
A: Key statistics from one example SMT dataset for VP16. Each cell line was imaged on two days and the data were combined for analyses.
B: Cell-wise mean posteriors from state array inference (Methods, saspt). Each row represents the diffusion spectrum from one cell as a normalized heatmap.
C: Jump resampling experiment (Methods), sampling 1-100000 jumps from the whole dataset over 1000 bootstrapping replicates. Orange lines: medians; boxes: Q1-Q3; whiskers: Q1–1.5 IQR and Q3+1.5 IQR.
D: Variance of jumps from jump resampling experiment. Each point represents the variance of the 1000 bootstrapping replicates, sampled in three different ways (Methods).
E: Minimum values from (D), summarizing sources of variance in this dataset. Cell-to-cell variability is about two orders of magnitude larger than day-to-day variability in this dataset.

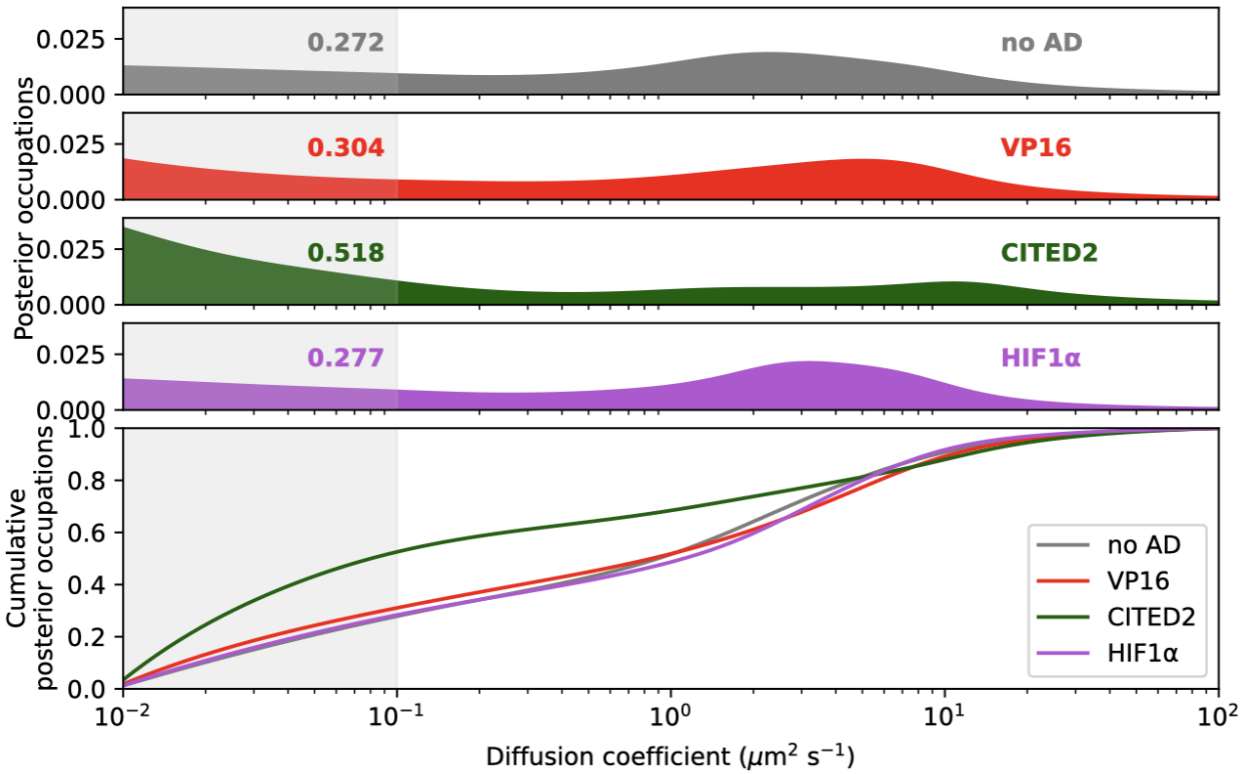

Figure 2—figure supplement 3: Diffusion spectra of activation domain-synthetic TF constructs in WT U2OS cells

WT U2OS cells without an integrated reporter locus were electroporated (Methods) with plasmids carrying different activation domain-synthetic TF constructs and imaged. Diffusion spectra are shown as in Figure 2.

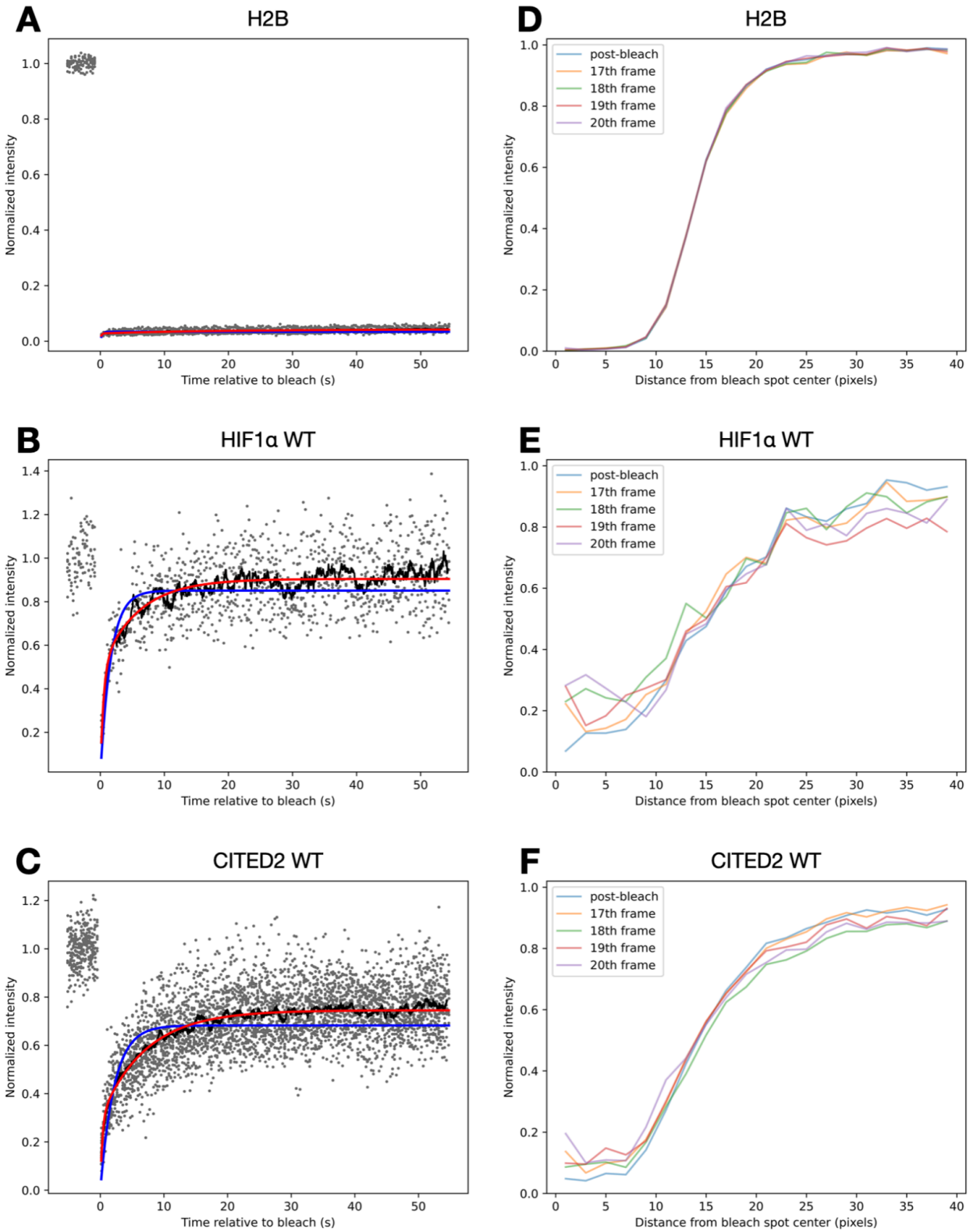
A
H2B
Normalized intensity
Time relative to bleach (s)
D
H2B
post-bleach
17th frame
18th frame
19th frame
20th frame
Normalized intensity
Distance from bleach spot center (pixels)
B
HIF1α WT
Normalized intensity
Time relative to bleach (s)
E
HIF1α WT
post-bleach
17th frame
18th frame
19th frame
20th frame
Normalized intensity
Distance from bleach spot center (pixels)
C
CITED2 WT
Normalized intensity
Time relative to bleach (s)
F
CITED2 WT
post-bleach
17th frame
18th frame
19th frame
20th frame
Normalized intensity
Distance from bleach spot center (pixels)

Figure 2—figure supplement 4: FRAP curves for histone H2B, HIF1α-synthetic TF, and CITED2-synthetic TF

A: Aggregate FRAP recovery curves showing a rolling-mean average (black line) and fits to a single-exponential line in blue and double-exponential line in red (Methods) for cells expressing H2B-HaloTag.

B: as in (A) for HIF1α-WT.

C: as in (A) for CITED2-WT.

Single-exponential fits to synthetic TF recoveries were poor.

D: Normalized radial bleach profiles (Methods) for cells expressing an H2B control. For the five frames immediately after the bleaching period, a radial profile centered at the bleach spot center is plotted and normalized between 0 and 1. The pixel size is 105.46875 nm. There are no obvious bleach spot shape changes as fluorescence recovers during photobleaching.

E: as in (D) for cells expressing HIF1α-WT synthetic TF.

F: as in (D) for cells expressing CITED2 AD synthetic TF.

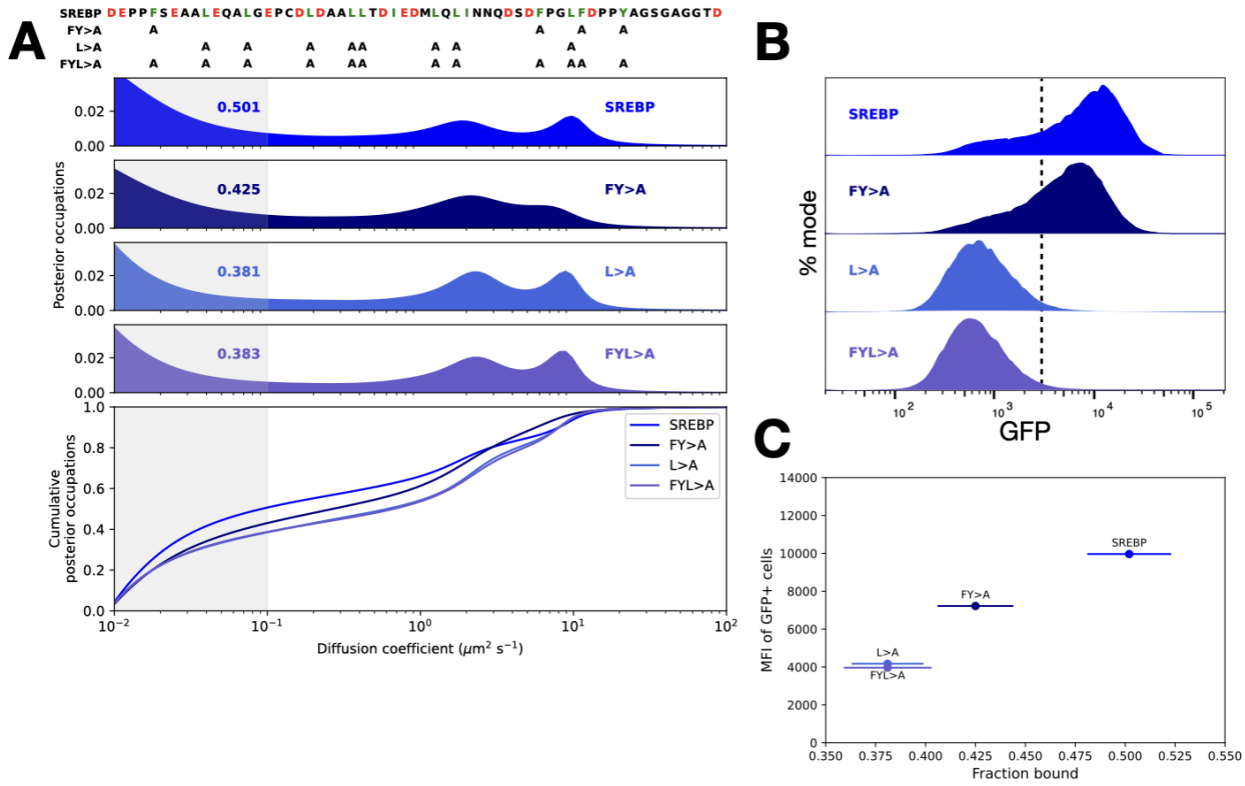

Figure 3—figure supplement 1: An additional allelic series with cholesterol TF SREBP's activation domain

A: Top: sequence of the WT SREBP activation domain appended to the synthetic transcription factor, and alanine mutations for three mutants of the SREBP activation domain. Bottom: diffusion spectra of cells expressing the labeled SREBP activation domain-synthetic TF constructs.

B: Flow cytometry distributions of GFP reporter expression in cells expressing various SREBP activation domains after 24 hours of estradiol induction.

C: Mean (geometric) fluorescence intensity of GFP-positive cells versus fraction bound for the SREBP constructs. Horizontal error bars denote standard deviation of bootstrapping replicates. Fraction bound correlates with mean fluorescence intensity in these four alleles.

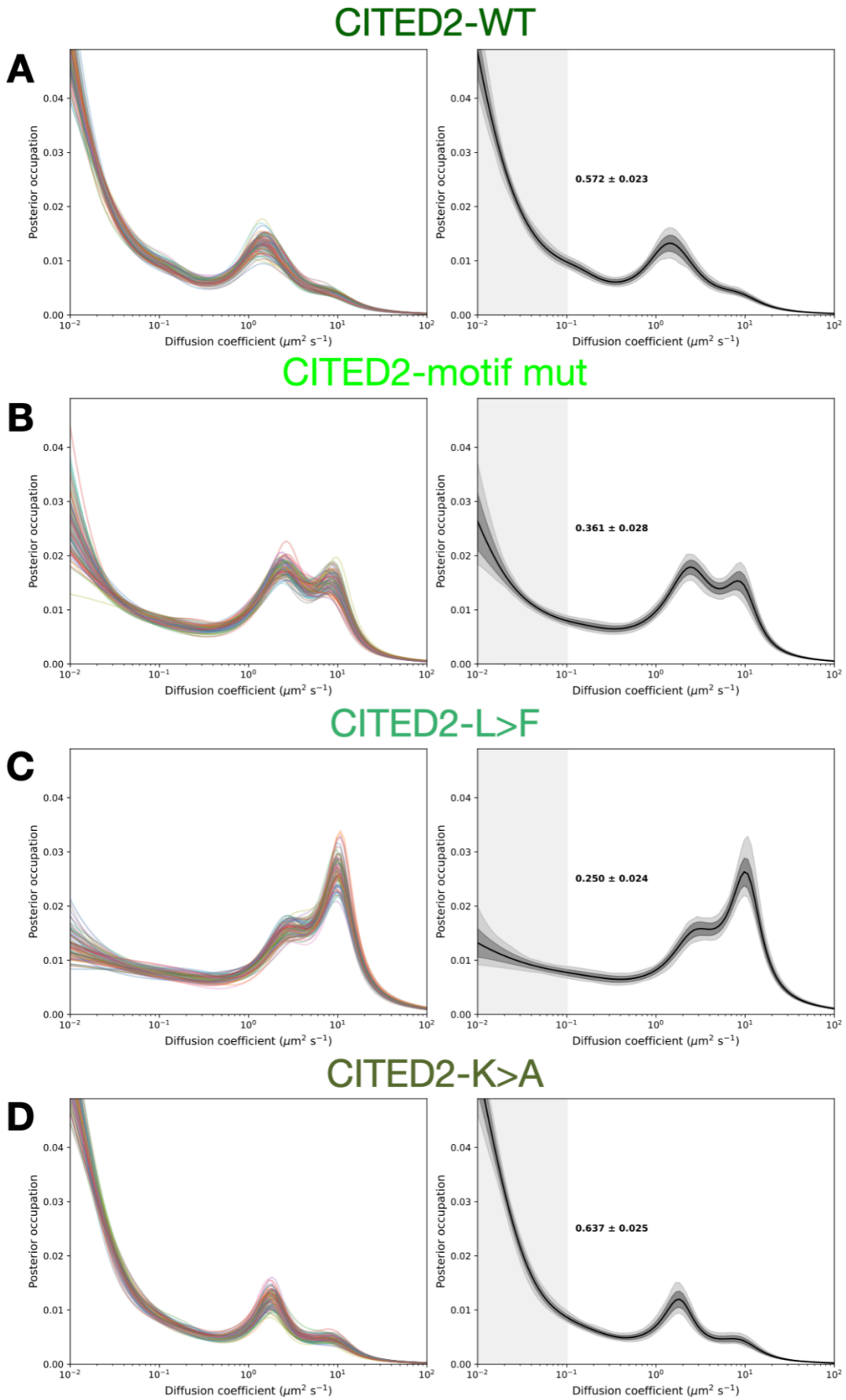
CITED2-WT
A
0.572 ± 0.023
CITED2-motif mut
B
0.361 ± 0.028
CITED2-L>F
C
0.250 ± 0.024
CITED2-K>A
D
0.637 ± 0.025
Posterior occupation
Diffusion coefficient (μm² s⁻¹)

Figure 3—figure supplement 2: Example outputs from a cell-wise bootstrapping scheme to estimate error in SMT diffusion spectra

Left panels: plots showing all 96 bootstrapping replicate spectra (Methods) as individual lines. Right panels: plots showing the mean of the bootstrapping replicates (solid lines), their standard deviations (dark gray shading), and their 95% confidence intervals (light gray shading). Numbers are the bootstrapping bound-fraction means and their standard deviations. **A**: CITED2-WT; **B**: CITED2-motif mut; **C**: CITED2-L>F; **D**: CITED2-K>A

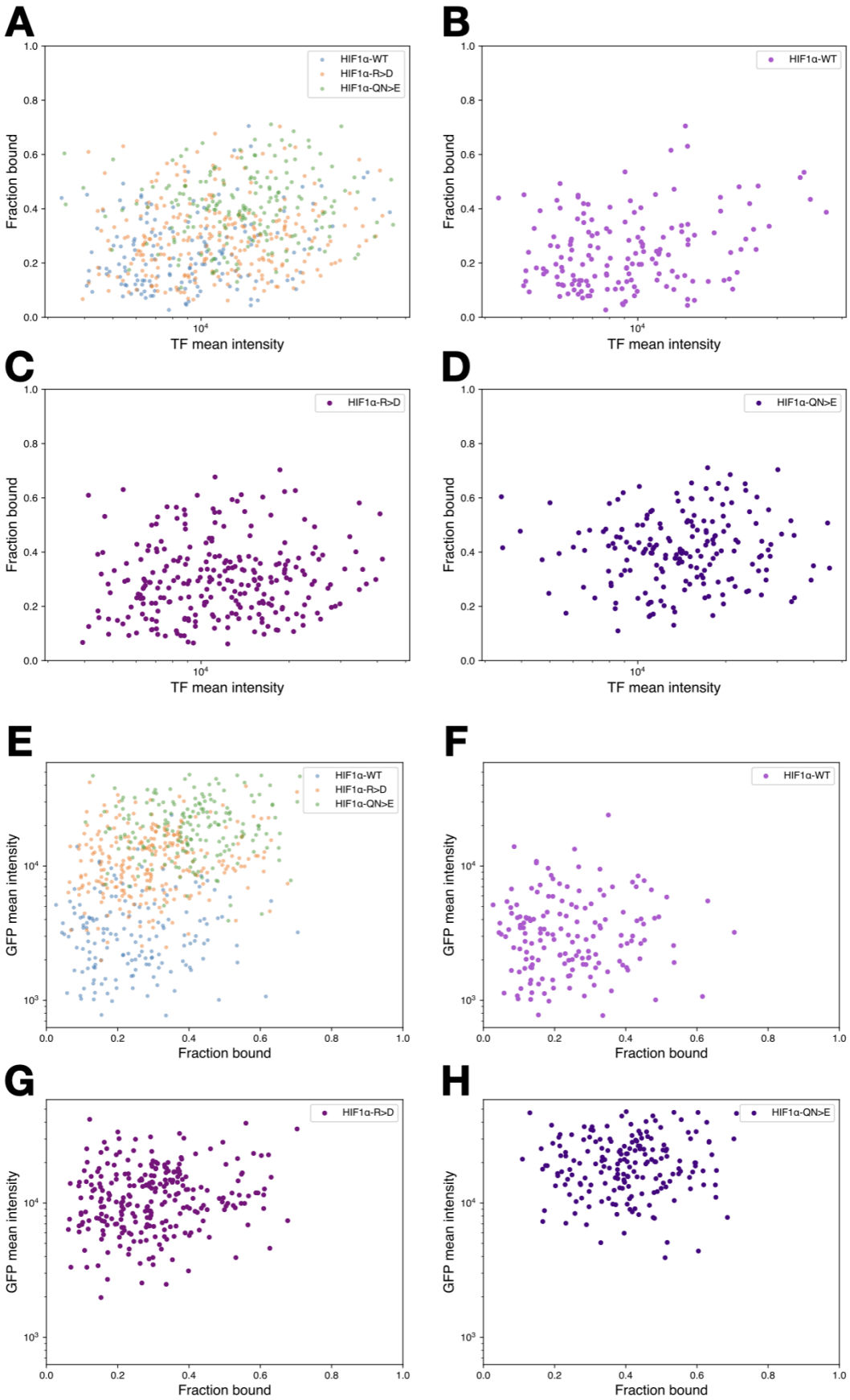
A
B
C
D
E
F
G
H
HIF1α-WT
HIF1α-R>D
HIF1α-QN>E
Fraction bound
TF mean intensity
GFP mean intensity
Fraction bound

Figure 3—figure supplement 3: Cell-wise relationships between chromatin-bound fraction, TF expression, and reporter output

A-D: Scatterplots of fraction bound measured by SMT, versus TF abundance, mean intensity in the HaloTag-ligand dye channel. Each point represents data from a single cell and is colored according to the legends. There is no obvious relationship between TF abundance and fraction bound on a cell or population level.

E-H: Scatterplots of mean intensity in the GFP channel versus fraction bound. Each point represents data from a single cell plotted on the same axes and colored according to the legends in the upper right. Cell lines expressing synthetic TFs adopt different distributions for both fraction bound and reporter expression, but neither parameter predicts the other in individual cells.

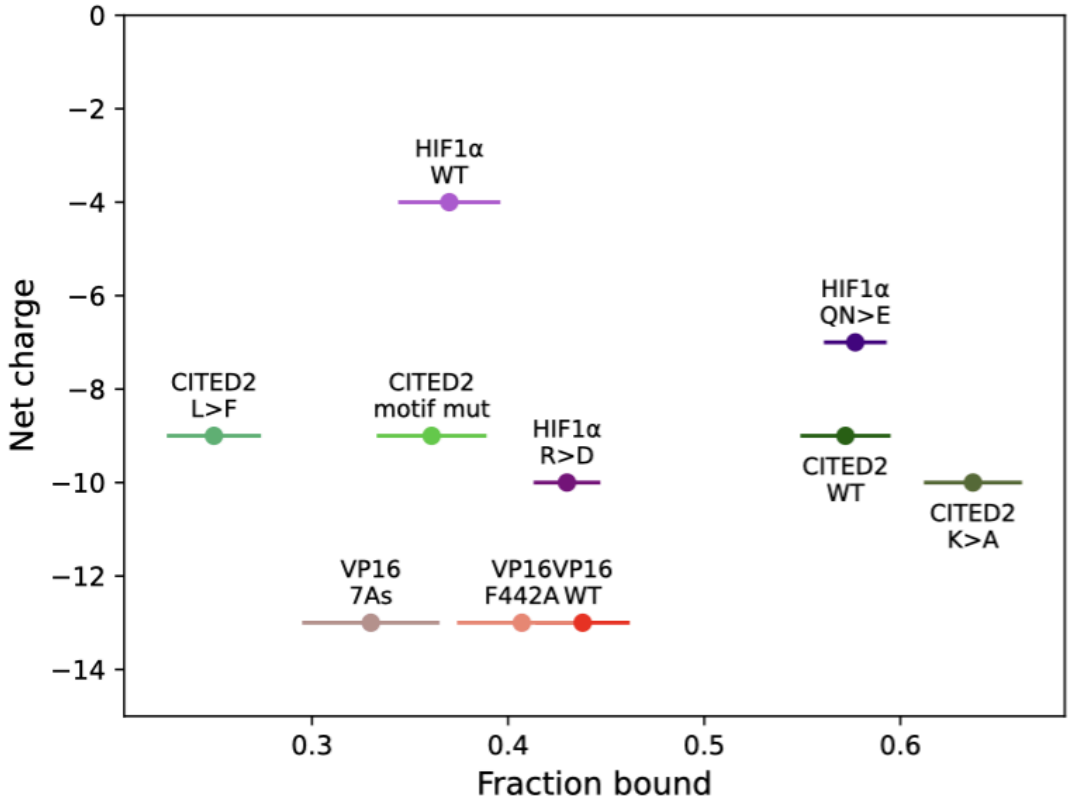

Figure 3—figure supplement 4: Activation domain net charge and fractions bound for constructs in Figure 3

Net activation domain charges are defined as the number of K and R residues minus the number of D and E residues. Net charges are plotted against fractions bound for each activator, as in Figure 3. There is no obvious relationship between net charge and bound fraction.

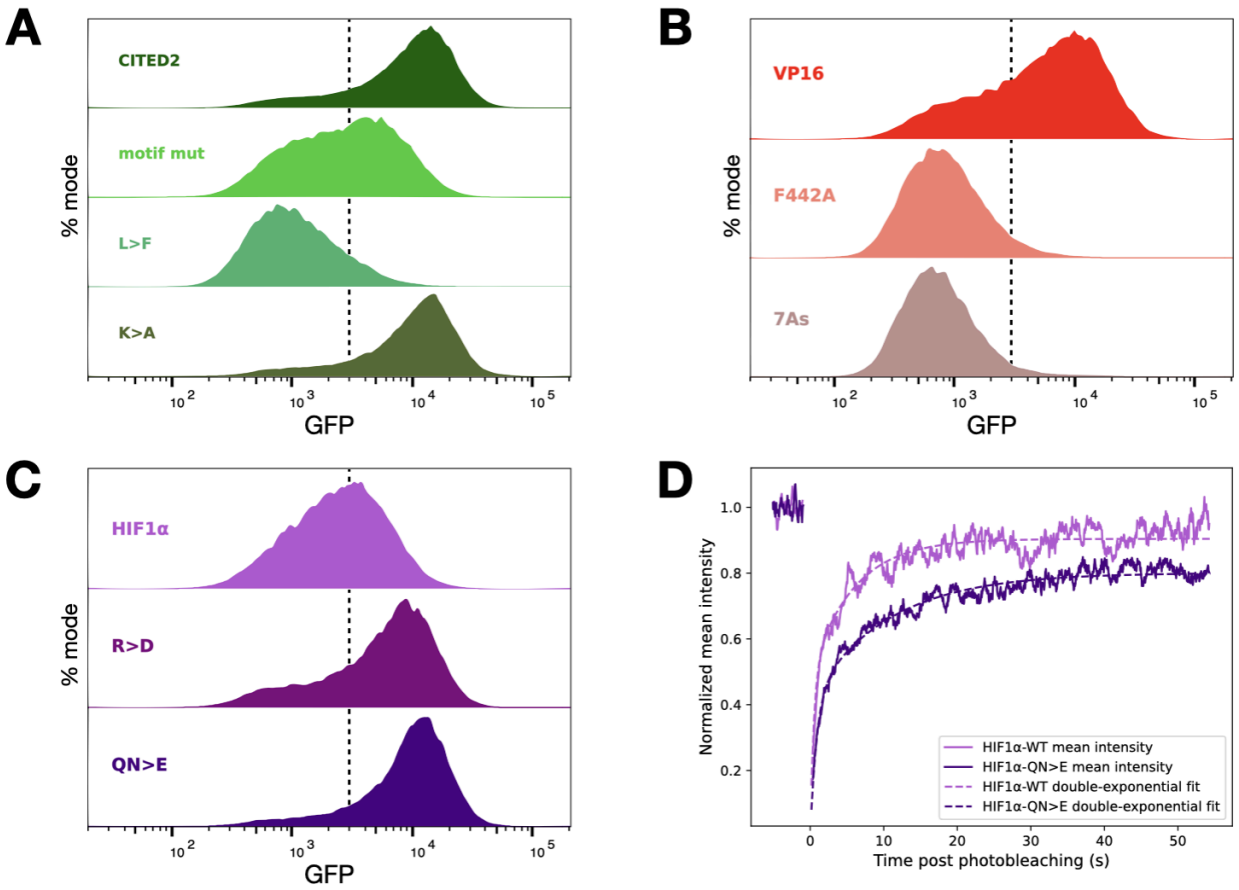

Figure 3—figure supplement 5: Mutations in activation domains change reporter activity and FRAP recovery

A: Flow cytometry measurement of GFP reporter expression after 24 hours of estradiol induction for cells expressing CITED2 alleles appended to the synthetic TF. The CITED2-WT curve is repeated from Figure 2B.

B: as in (A) for VP16 alleles. The VP16-WT curve is repeated from Figure 2B.

C: as in (A) for HIF1α alleles. The HIF1α-WT curve is repeated from Figure 2B.

D. Aggregate FRAP recovery curves (rolling averages, solid lines) for HIF1α and superactive allele of HIF1α (QN>E). Double-exponential fits are plotted as dashed lines. HIF1α-WT FRAP curve also appears in Figure 2D.

	fast-recovering fraction	fast recovery time (sec)	slow-recovering fraction	slow recovery time (sec)
CITED2	0.297	0.319	0.448	7.03

HIF1α-WT	0.487	0.49	0.417	5.77
HIF1α-QN >E	0.417	0.854	0.384	10.5
H2B*	0.028	0.134	0.0144	19.8

Supplementary Table 1: FRAP parameters extracted from a double-exponential recovery model

FRAP population fractions and recovery times for cells expressing various synthetic TFs and H2B. Stronger activation domains have longer slow-recovery times, indicating longer residence times bound to chromatin. *Note that >95% of H2B molecules do not recover on the timescale of the FRAP experiment.

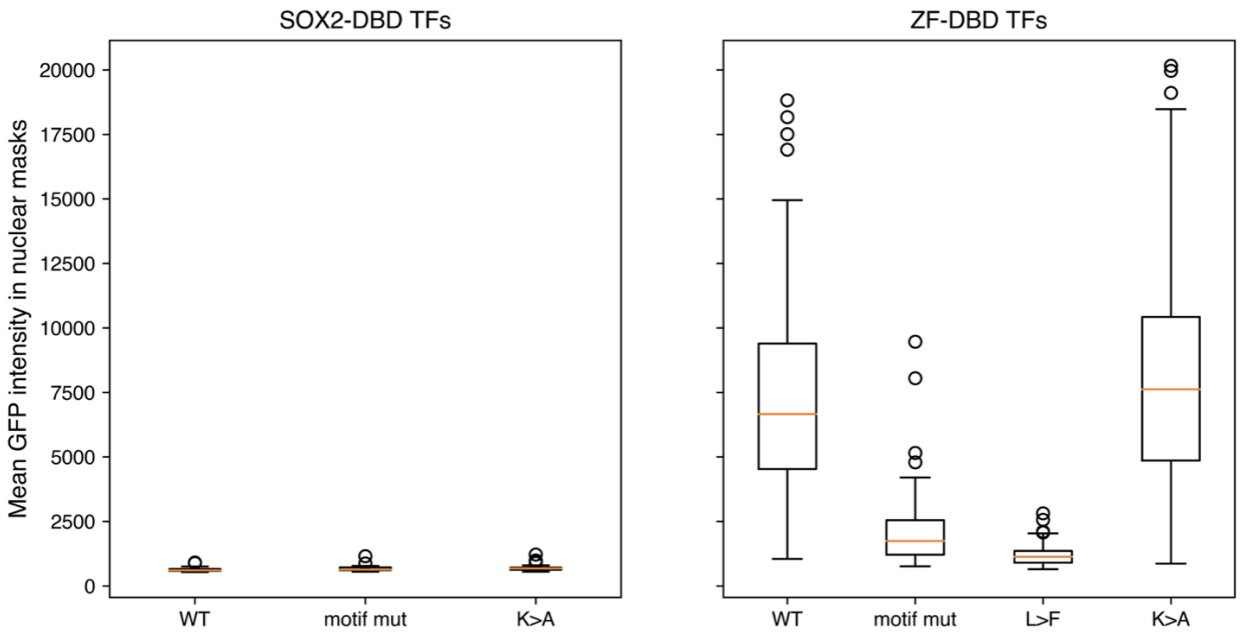

Figure 4—figure supplement 1: AAVS1-integrated GFP reporter with synthetic ZF binding sites is not activated by SOX2DBD-activation domain constructs
Fluorescence intensities from the GFP channel of microscope images were quantified from experiments in Figure 4A and compared to those in Figure 3A. Orange lines: medians; boxes: Q1-Q3; whiskers: Q1–1.5 inter-quartile range and Q3+1.5 inter-quartile range.
Left: GFP intensities from cells with SOX2DBD fused to various mutants of CITED2. Right: GFP intensities from cells with the synthetic ZF DBD fused to various mutants of CITED2.

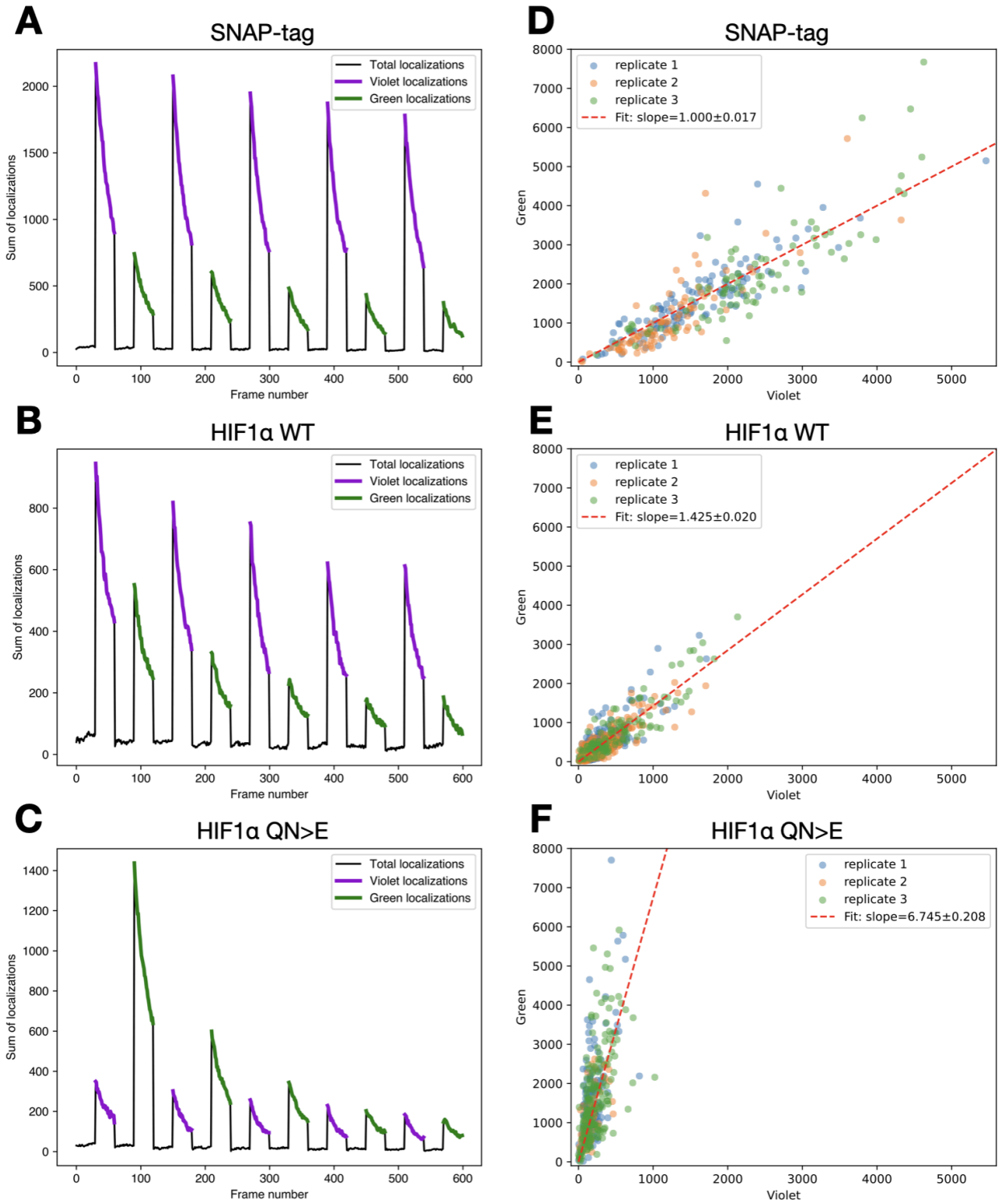
A
SNAP-tag
Total localizations
Violet localizations
Green localizations
Sum of localizations
Frame number
B
HIF1α WT
Total localizations
Violet localizations
Green localizations
Sum of localizations
Frame number
C
HIF1α QN>E
Total localizations
Violet localizations
Green localizations
Sum of localizations
Frame number
D
SNAP-tag
replicate 1
replicate 2
replicate 3
Fit: slope=1.000±0.017
Green
Violet
E
HIF1α WT
replicate 1
replicate 2
replicate 3
Fit: slope=1.425±0.020
Green
Violet
F
HIF1α QN>E
replicate 1
replicate 2
replicate 3
Fit: slope=6.745±0.208
Green
Violet

Figure 5—figure supplement 1: PAPA analysis intermediates
A: For one PAPA replicate imaging cells expressing SNAP-tag, the number of localizations as a function of frame number is plotted as a black line. Localizations immediately following a violet or green pulse (and considered reactivated for downstream analyses) are plotted as bold violet and green lines, respectively.
B: as in (A) for cells expressing HIF1α WT.
C: as in (A) for cells expressing HIF1α QN>E.
D: Cell-wise normalized PAPA ratios (Methods) are plotted across three replicates for cells expressing SNAP-tag and colored according to the legend. A line whose y-intercept is zero is fit to these points and plotted as a dashed red line.
E: as in (D) for cells expressing HIF1α WT.
F: as in (D) for cells expressing HIF1α QN>E.

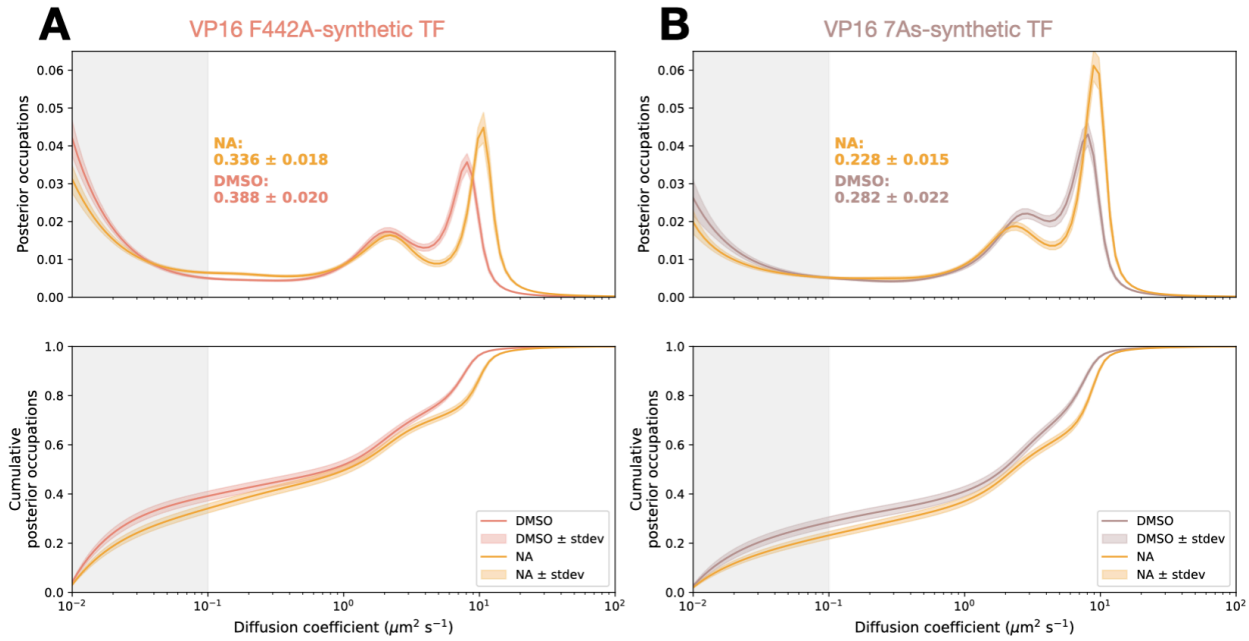

Figure 6—figure supplement 1: Drug perturbations on the synthetic TF bearing mutants of the VP16 activation domain
A: Diffusion spectra (top) and cumulative distributions (bottom) for VP16 F442A-synthetic TF-expressing cells treated for two hours with norstictic acid or vehicle (DMSO). Shading indicates standard deviation of bootstrapping trials.
B: as in (A) for VP16 7As-synthetic TF.

Figure	Sample	Fraction bound	Number of cells	Number of trajectories	Number of jumps	Number of detections
2A	no AD	0.408	70	52671	50823	103494
2A	VP16-WT	0.484	193	91507	143101	234608
2A	CITED2-WT	0.585	210	115059	178328	293387
2A	HIF1α-WT	0.388	218	125572	121533	247105
2—FS 3*	no AD (transient, no cognate binding sites)	0.272	25	13489	12209	25698
2—FS 3*	VP16-WT (transient, no cognate binding sites)	0.304	24	20342	13708	34050
2—FS 3*	CITED2-WT (transient, no cognate binding sites)	0.518	26	15374	14289	29663
2—FS 3*	HIF1α-WT (transient, no cognate binding sites)	0.277	37	21968	18410	40378
3A	CITED2-WT	0.572	80	35993	73211	109204
3A	CITED2-motif mut	0.366	75	37910	43322	81232
3A	CITED2-L>F	0.25	69	28887	20545	49432
3A	CITED2-K>A	0.642	99	51950	100436	152386
3A	VP16-WT	0.435	91	49324	65239	114563
3A	VP16-F442A	0.403	66	39530	55621	95151
3A	VP16-7As	0.334	77	42715	51831	94546
3A	HIF1α-WT	0.373	158	74770	76949	151719
3A	HIF1α-R>D	0.428	261	132131	189831	321962
3A	HIF1α-QN>E	0.577	185	110499	163823	274322
3—FS 1A	SREBP-WT	0.501	170	107390	125127	232517
3—FS 1A	SREBP-FY>A	0.425	121	69256	114124	183380
3—FS 1A	SREBP-L>A	0.381	183	103969	138686	242655
3—FS 1A	SREBP-FYL>A	0.383	156	97062	128329	225391
4A	CITED2-WT (SOX2 DBD)	0.318	69	48771	87998	136769
4A	CITED2-motif mut (SOX2 DBD)	0.267	51	37010	67565	104575
4A	CITED2-K>A (SOX2 DBD)	0.612	63	65684	77811	143495

4B*	HIF1α-WT (full-length)	0.159	21	11325	20598	31923
4B*	HIF2α-WT (full-length)	0.313	20	13419	25661	39080
4B*	HIF1α/2α chimera	0.325	19	12637	20841	33478
4B*	HIF2α/1α chimera	0.209	20	15085	25953	41038
4C*	HIF1α-WT (full-length)	0.185	44	26897	25135	52032
4C*	HIF1α-QN>E (full-length)	0.273	45	34697	43392	78089
5C	HIF1α-WT, violet-reactivated	0.693	410	20509	74171	94680
5C	HIF1α-WT, green-reactivated	0.697	258	11552	40758	52310
5D	HIF1α-R>D, violet-reactivated	0.6	100	4634	17003	21637
5D	HIF1α-R>D, green-reactivated	0.685	132	5938	22466	28404
5E	HIF1α-QN>E, violet-reactivated	0.6	220	10543	36273	46816
5E	HIF1α-QN>E, green-reactivated	0.719	282	13217	45646	58863
6A	VP16-WT + DMSO	0.436	260	119319	176271	295590
6A	VP16-WT + NA	0.399	385	352093	308108	660201
6B	no AD + DMSO	0.389	69	33395	44061	77456
6B	no AD + NA	0.351	63	43238	41587	84825
6C	VP16-WT + DMSO	0.414	82	42678	51185	93863
6C	VP16-WT + A485	0.486	79	46383	63874	110257
6D	no AD + DMSO	0.389	69	33395	44061	77456
6D	no AD + A485	0.301	71	40742	38356	79098
6E	VP16-WT + DMSO	0.452	138	67534	97622	165156
6E	VP16-WT + BAFi	0.328	122	55005	76245	131250
6F	no AD + DMSO	0.389	69	33395	44061	77456
6F	no AD + BAFi	0.356	62	29280	37968	67248
6—FS 1A	VP16-F442A + DMSO	0.388	344	169668	214748	384416
6—FS 1A	VP16-F442A + NA	0.336	187	155049	115549	270598
6—FS 1B	VP16-7As + DMSO	0.282	262	133015	161375	294390
6—FS 1B	VP16-7As + NA	0.228	205	159420	128855	288275

Supplementary Table 2: Summary of SMT measurements

Fraction bound, number of cells imaged across all replicates, number of trajectories, number of jumps, and number of detections for all SMT experiments reported in this article. All tabulated values are post-filtering (Methods: SMT and PAPA-SMT analysis). Number of trajectories and number of detections include singlets: detections that were not linked to any other detection and do not contribute any data to downstream analyses but have their own “trajectory” index. * indicates datasets acquired without an automated nucleus-finding macro.

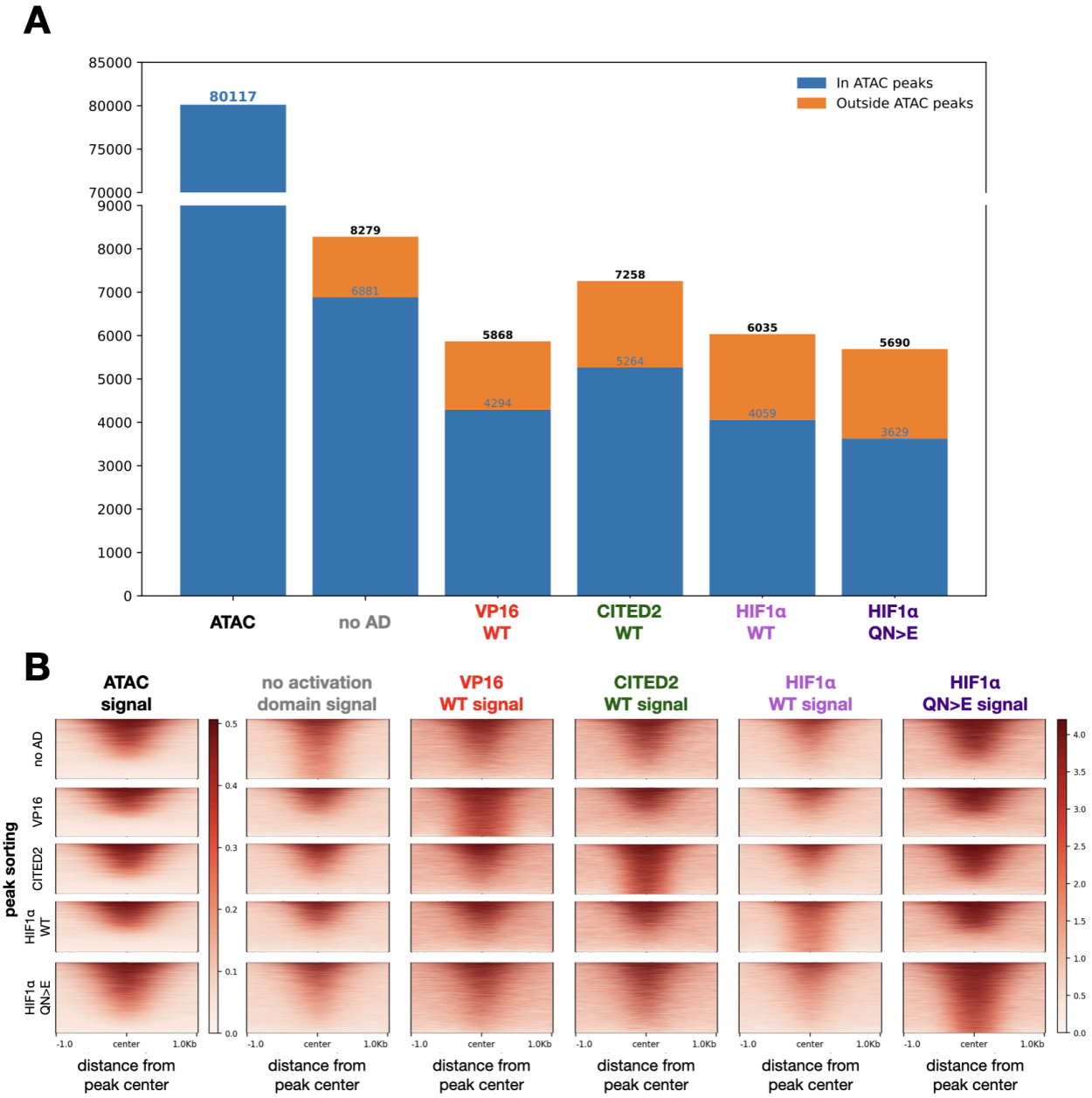

Figure 7—figure supplement 1: Synthetic TFs bearing various activation domains generally bind to similar, open regions of the genome

A: Stacked barplot quantifying ATAC-seq and CUT&RUN peaks overlapping (blue) and not overlapping (orange) ATAC-seq peaks for various activation domain-synthetic TFs.

B: ATAC-seq signal and synthetic TF binding signal is plotted in descending peak strength order for the TF shown labeled on the left. The five synthetic TFs share a color scale; the ATAC-seq signal uses a separate scale. The synthetic TFs with various activation domains generally bind to similar regions of the genome, especially those within ATAC-accessible regions.

Materials and methods

U2OS cell culture

U2OS cells (osteosarcoma from a 15-year-old human female) were originally obtained from the UC Berkeley Cell Culture facility. Cells were maintained at 37°C in a humidified atmosphere with 5% CO_2 and cultured in reconstituted DMEM containing 4.5 g/L glucose (Thermo 12800082) supplemented with 9.1% fetal bovine serum ("FBS", HyClone), L-glutamine (Sigma), GlutaMax (Thermo), and 100 U/mL penicillin-streptomycin (Thermo). Cells were generally passaged every three days by splitting 1:8, using 0.25% trypsin to facilitate detachment.

Cell lines used in this study tested negative for mycoplasma about monthly by PCR (https://bitesizebio.com/23682/homemade-pcr-test-for-mycoplasma-contamination/). Cells were tested to be U2OS cells with STR profiling at the UC Berkeley Cell Culture facility.

For imaging experiments, cells were plated the evening prior to imaging to achieve 60–80% confluency on the day of imaging. Cells were grown on glass-bottom dishes (MatTek P35G-1.5-14-C) in phenol-red-free DMEM containing 4.5 g/L glucose and supplemented with 9% FBS and 100 U/mL penicillin-streptomycin ("imaging medium").

U2OS cell line generation

To generate the reporter cell line, U2OS cells were transfected in 6-well dishes using Lipofectamine™ 3000, with 3 µg of DNA and 6 µL of Lipofectamine™ 3000 per well. Each well received 1 µg of a combined Cas9 and sgRNA plasmid targeting the AAVS1 locus (Addgene plasmid #227272) and 2 µg of repair template containing the reporter locus, similar to that of the previously-described construct (Staller et al., 2022).

The reporter construct is based on a published reporter (Addgene #176294), but we replaced puromycin resistance with blasticidin resistance, added VKYY to the start of the GFP to boost translation (Verma et al., 2019), inserted a small t intron, and inserted a WPRE before the SV40 poly(A) signal.

Two days after transfection, cells were passaged onto a 10 cm dish and selected with blasticidin (Fischer A1113903) at 5 µg/mL. When this dish was confluent, single clones were isolated by limiting dilution into 96-well plates and sequence-validated to

have at least one copy of the reporter locus by PCR and Sanger sequencing. Clones were also tested by transient transfection of a VP16 synthetic TF by measuring fold-induction in response to estradiol induction. We picked the most robustly induced clone for this study. Cells were maintained in media containing 5 μg/mL blasticidin.

All synthetic zinc-finger- and SOX2DBD-bearing constructs were cloned using Gibson Assembly and verified via whole-plasmid sequencing (Plasmidsaurus). Starting with a published synthetic TF (Addgene #176293), we moved the TF into PiggyBac backbone with a L30 promoter, replaced mScarlet with HaloTag, added a V5 tag, and replaced the neomycin resistance with puromycin resistance. These constructs were stably integrated into the reporter clone described above. For integrations, we transfected 2 μg of a synthetic construct with 1 μg of a vector expressing Super PiggyBac Transposase (Yusa et al., 2011) in this reporter clone. Two days after transfection, we passaged cells onto a 10 cm dish and selected cells with puromycin (Invivogen) at 1 μg/mL. We continued passaging these cells for at least two weeks before proceeding with experiments. Cells were maintained in media containing 5 μL/mL blasticidin and 1 μg/mL puromycin.

Selection of activation domain mutations

We selected mutations that strongly changed activation domain activity in our published assay (Staller et al., 2022). The QN>E mutation prevents hydroxylation, a modification which normally destabilizes the protein and interferes with p300 binding (Hewitson et al., 2002; Lando et al., 2002a, 2002b).

Nucleofection and drug treatments

For Figures 4B and C, U2OS cells were electroporated using a homemade buffer (Danner, 2020) and the X-001 protocol of the Lonza Nucleofector II. This method mitigates autofluorescence artifacts from lipid-based transfection reagents. One million U2OS cells were electroporated with previously-described constructs (Chen et al., 2022) and treated with deferoxamine mesylate salt (Sigma D9533) at 100 μM overnight.

For Figures 5A, D and Figure 5—figure supplement 1, uninduced cells were treated for 2 hours with 10 μM norstictic acid (Santa Cruz Biotechnology) or the equivalent DMSO. These cells were stained with HaloTag ligand (as in “Sample preparation for imaging experiments”) and induced with 1 μM β-Estradiol (Sigma E2758; “estradiol”) immediately before imaging.

For Figure 5B and E, uninduced cells were treated for 2 hours with 10 μM A485 (Fischer) or the equivalent DMSO. These cells were stained with HaloTag ligand (as in "Sample preparation for imaging experiments") and induced with 1 μM estradiol immediately before imaging.

For Figure 5C and F, uninduced cells were treated for 2 hours with 10 μM BRM/BRG1 ATP Inhibitor-1 compound 14 (MedChemExpress; "BAFi") or the equivalent DMSO. These cells were stained with HaloTag ligand (as in "Sample preparation for imaging experiments") and induced with 1 μM estradiol immediately before imaging.

Except for treatments noted above in this section, cells in all other conditions were treated with 1 μM estradiol for 12-16 hours the night before they were imaged for SMT.

For all flow cytometry experiments, cells were treated with 1 μM estradiol for 24 hours.

Incucyte live-cell imaging

To assay reporter induction at fine time intervals, we used the Incucyte S3 system to acquire images every two hours post estradiol induction. The day before the experiment, cells were plated at around 25% confluence. The day of the experiment, cells were induced with 1 μM estradiol, and the first image was taken about five minutes later (as the 0 hour time point).

Images in phase and the green channel (to quantify GFP) were acquired with the 10x objective. The Incucyte S3 software was used to segment cells and quantify the amount of GFP in each cell. These amounts were used to draw an arbitrary gate separating GFP-positive and -negative cells. The percentage of GFP-positive cells were computed and plotted as a function of time using Python.

Flow cytometry

The day of the assay, cells were stained for ten minutes with 35 nM of JFX650-HaloTag ligand and 10 μM Hoechst 33342 (Thermo), rinsed once with imaging medium, and incubated in imaging medium for 25 minutes. Cells were lifted using 0.25% trypsin, quenched with imaging medium, and filtered through a cell strainer to remove clumps.

Flow cytometry was conducted on a BD Bioscience LSR Fortessa in the UC Berkeley Flow Cytometry Core. Conditions presented together as panels were

collected on the same day with the same voltages. These voltages were not always kept consistent from day-to-day, as daily CST calibration often changed cytometer baselines. 30,000 measurements were made for each condition.

Data were analyzed using FlowJo, with consistent gating applied across conditions that are presented together in a panel. The reporter fluorescence distributions were frequently bimodal, so we quantified reporter activity in two ways. First, we used the fraction of cells that were GFP positive, but this metric had a limited dynamic range. Second, we used the mean fluorescence intensity (MFI) of GFP-positive (GFP+) cells, which had a larger dynamic range.

Single-molecule tracking (SMT) movie acquisition

The day of imaging, cells were stained for five minutes with JFX650-HaloTag ligand (generously gifted by the Lavis lab), added to a final concentration of 5 nM and 2 μM Hoechst 33342 (Thermo), rinsed once with imaging medium, and incubated in imaging medium for ten minutes. The dishes were rinsed one more time, replenished with imaging medium, and mounted on the microscope with Nikon immersion oil Type F.

The microscope used for SMT is as previously described (Hansen et al., 2018). In brief, this imaging setup consisted of a Nikon TI microscope fitted with a 100X/NA 1.49 oil-immersion TIRF objective, a motorized mirror, a Perfect Focus system, an EM-CCD camera, and an incubation chamber maintained at 37°C with a humidified 5% CO_2 atmosphere. The laser launch includes lasers of the following wavelengths: 405 nm (140 mW, OBIS, Coherent), 488 nm, 561 nm, and 639 nm (all 1 W, Genesis, Coherent). Laser intensities were regulated using an acousto-optic tunable filter (AA Opto-Electronic, AOTFnC-VIS-TN) and triggered via the camera's TTL exposure output signal. Lasers were delivered to the microscope through an optical fiber, reflected by a quad-band dichroic mirror (405 nm/488 nm/561 nm/633 nm, Semrock), and focused at the back focal plane of the objective. The incident laser angle was adjusted to achieve highly inclined laminated optical sheet (HILO) illumination (Tokunaga et al., 2008). Emission light was filtered using the appropriate Semrock single band-pass filters.

For the diffusion spectra shown in each panel, all conditions were imaged on the same day to minimize day-to-day variability. A second replicate was imaged on a different day, and the data from both days were pooled to generate the reported spectra.

All experiments except those in Figures 4B, C and Figure 2—figure supplement 3 used an automated imaging scheme derived from one previously described in (Walther et al., 2024). Briefly, custom NIS Elements Macro Language and Python scripts instructed the microscope to raster over a coverslip, taking 81.92 µm x 81.92 µm images at each grid point. Cell presence in a field was determined using StarDist segmentation (Schmidt et al., 2018) in the Hoescht channel; images in additional channels of interest (GFP: 488 nm, JFX650: 639 nm) were also acquired. If cells were identified, one was randomly selected for imaging at 7.48 ms using the following protocol: 1200 frames with 2 ms stroboscopic illumination of the 639 nm laser (1 W, 100%), followed by 1200 frames with 2 ms stroboscopic illumination of the 639 nm laser (1 W, 100%) combined with 30% 405 nm laser power during camera transition intervals, and finally 1200 frames with 2 ms stroboscopic illumination of the 639 nm laser (1 W, 100%) combined with 60% 405 nm laser power during camera transition intervals. The 405 nm laser pulses during transition times were used to reactivate dark JFX650 fluorophores (Endesfelder and Heilemann, 2015) while minimizing background contribution by the laser pulse itself.

Proximity-assisted photoactivation (PAPA) SMT movie acquisition

The day of imaging, cells were stained for ten minutes with 50 nM JFX549-HaloTag ligand and either 5 nM JFX650-SNAP-tag ligand (for SNAP-tag control conditions) or 50 nM JFX650-SNAP-tag ligand (for all other conditions; all dyes were generous gifts from the Lavis lab). Dishes were rinsed once with imaging medium and incubated in imaging medium for 15 minutes. The dishes were rinsed once more, replenished with imaging medium, and mounted on the microscope (same as described in “Single-molecule tracking (SMT) movie acquisition”) with Nikon immersion oil Type F.

All PAPA experiments used the microscope setup and automation scheme previously described in “Single-molecule tracking (SMT) movie acquisition” with the following differences:

We used the 561 nm laser to measure p300-HaloTag nuclear intensities, and only cells with mean intensity values between 2000 and 20000 were considered for imaging. StarDist-segmented objects with an area less than 3500 pixels (89.6 μm^2) or more than 7000 pixels (179.2 μm^2) were rejected. We also acquired images using the 639 nm laser for the SNAP-tagged proteins’ expression levels and only considered nuclei with mean intensities above 5000. If more than one suitable cell was found for

imaging, we selected the largest cell to image to recover the most localizations possible.

After a cell was selected by this automated scheme, the imaging macro shrank the region-of-interest to encapsulate the nucleus and applied the 639 nm laser at 100% intensity for five seconds to “shelve” fluorescent SNAP-tagged molecules. Then, we used the following illumination sequence with eight phases (all 7.48 ms frames):

1. 200 frames of 1 W 639 nm laser at 100% intensity: these frames are not saved and serve to shelve SNAP-tagged molecules before the next reactivation pulse.
2. 30 frames of 1 ms stroboscopic 1 W 639 nm laser at 100% intensity: these frames are saved and are a readout for “spontaneous reactivation”, reactivation of molecules that is independent of a green or violet pulse.
3. 2 frames of 405 nm laser at 100% intensity: this pulse of violet light reactivates “shelved” SNAP-tagged molecules regardless of whether or not they are complexed. These frames are not saved.
4. 30 frames of 1 ms stroboscopic 1 W 639 nm laser at 100% intensity: these frames are saved and read out the violet-reactivated molecules from the previous pulse.
5. 200 frames of 1 W 639 nm laser at 100% intensity: these frames are not saved and serve to shelve SNAP-tagged molecules before the next reactivation pulse.
6. 30 frames of 1 ms stroboscopic 1 W 639 nm laser at 100% intensity: these frames are saved and are a readout for “spontaneous reactivation”, reactivation of molecules that is independent of a green or violet pulse.
7. 50 frames of 100 mW 561 nm laser at 100% intensity: this pulse of green light reactivates SNAP-tagged molecules dependent on their proximity to p300-HaloTag. These frames are not saved.
8. 30 frames of 1 ms stroboscopic 1 W 639 nm laser at 100% intensity: these frames are saved and read out the green-reactivated molecules from the previous pulse.

This sequence is repeated five times before the cell-finding phase of the macro starts again.

SMT and PAPA-SMT analysis

Spots were detected, subpixel-localized, and linked into trajectories using algorithms within the open-source Python package quot (https://github.com/alecheckert/quot) using the following parameters:

'filter': {'start': 0, 'method': 'identity'}, 'detect': {'method': 'llr', 'k': 1.5, 'w': 11, 't': 18.0}, 'localize': {'method': 'ls_int_gaussian', 'window_size': 11, 'sigma': 1.5, 'ridge': 0.0001, 'max_iter': 10, 'damp': 0.3, 'camera_gain': 109.0, 'camera_bg': 470.0}, 'track': {'method': 'conservative', 'pixel_size_um': 0.16, 'search_radius': 1.0, 'max_blinks': 0, 'min_l0': 0.0}.

We segmented cell nuclei images with either StarDist (Schmidt et al., 2018) or cellpose (Stringer et al., 2021) as a starting point but found that manual QC and refining were necessary for accurate masking. This was done with a custom Python GUI (https://github.com/vinsfan368/qtpicker).

Only trajectories whose points lie entirely within one, and only one, curated mask were analyzed. For nuclei with more than six localizations per frame in at least one frame, we truncated frames from the beginning of the movie until all frames had fewer than seven localizations per frame. We then excluded cells with fewer than 100 displacements to ensure greater confidence in cell-wise posterior estimates. These three filters were post hoc choices and not pre-established exclusion criteria.

The resulting trajectories were analyzed using the open-source and previously-published Python package saspt (https://github.com/alecheckert/saspt; Heckert et al., 2022). We used the following inference parameters: focal_depth=0.7, sample_size=1000000, likelihood_type='rbme', splitsize=3, start_frame=0 (with the sample_size parameter being arbitrarily large to analyze all trajectories). For Figures 4B and C, we used the above parameters but replaced splitsize=3 with splitsize=8 to maintain consistency with our previously-published results (Chen et al., 2022).

In figures where errors are reported, we followed a similar scheme previously described in (Ferrie et al., 2024): for a dataset comprising n cells, we subsampled n random cells with replacement 96 times. For each of these trials, we pooled all trajectories from the n random cells, ran inference using the parameters described above, and noted the fractions bound. The bootstrapping means, standard deviations, and 95% confidence intervals are reported and/or plotted where indicated.

Quantifying sources of variance in SMT data

To quantitatively describe sources of variance (Figure 2—figure supplement 2) within our data in a non-model-dependent and computationally inexpensive way, we were inspired by (Driouchi et al., 2025). Briefly, we collate trajectories, noting the day on which they were imaged and the cell from which they were collected. We then decompose this data into individual displacements and subsample arbitrary numbers

(n) of these jumps 1000 times, noting the mean value of these 1000 trials. By varying both n and the sampling scheme, we can assess sources of variance. We sampled according to three schemes: (1, gray) n jumps from the entire pool of trajectories, which establishes the baseline and should follow the law of large numbers as n becomes larger; (2, blue) by picking one cell from the dataset and sampling n jumps from only that cell; and (3, orange) by picking an imaging day from the dataset and sampling n jumps imaged only on that day. When curves 2 and 3 diverge from 1, all variance with respect to n has been captured. We note that variability between fields-of-view could contribute to cell-to-cell variability, but given that most of our fields-of-view contained only one cell, we did not quantify this source of variability. We found in Figure 2—figure supplement 2 that cell-to-cell variability is about 100x higher than day-to-day variability.

Normalized PAPA ratio and confidence intervals

To calculate the normalized PAPA ratio (Figure 5B), we tallied green- and violet-reactivated molecules in PAPA movies and additionally controlled for spontaneous reactivation of molecules: green- and violet-independent reactivations that likely depend on the expression level of the SNAP-tagged protein in a given nucleus. To do this, we subtracted the number of spontaneously-reactivated molecules from the number of molecules reactivated by a proceeding green or violet pulse; e.g., molecules localized in phase 2 of the illumination sequence in “Proximity-assisted photoactivation (PAPA) SMT movie acquisition” were subtracted from those in phase 4, and molecules localized in phase 6 of this sequence were subtracted from those in phase 8. This yielded a corrected green-to-violet ratio for each cell measured.

Next, we divided these cell-wise corrected green-to-violet (G/V) ratios for each condition by the aggregate corrected G/V ratio of the SNAP-tag control imaged on the same day (Figure 5—figure supplement 1D-F). For example, if a cell expressing HIF1α AD-synthetic TF had a G/V ratio of 0.36 on a day the aggregate G/V ratio for SNAP-tag alone was 0.26, its normalized G/V ratio is 1.4.

Finally, we calculated the mean and derived error bounds for the normalized PAPA ratios by bootstrapping. For a condition comprising n cells (imaged over multiple days, but each normalized to their appropriate SNAP-tag control), we picked n cells from that condition with replacement and calculated the combined normalized G/V ratio of this pool. We repeated this 96 times and used this to derive 95% confidence intervals.

Fluorescence recovery after photobleaching (FRAP) movie acquisition

The day of imaging, cells were stained for five minutes with TMR-HaloTag ligand (Promega) added to a final concentration of 50 nM, rinsed once with imaging medium, and incubated in imaging medium for 10 minutes. The dishes were rinsed one more time, replenished with imaging medium, and mounted on the microscope with Immersol 518 F (Zeiss). The dish was then left to equilibrate thermally for about five minutes prior to imaging.

FRAP was conducted using a ZEISS LSM900 Airyscan 2 laser-scanning confocal microscope mounted on an inverted Axio Observer.Z1/7 platform and operated with ZEN 3.1 blue software. The system was equipped with a temperature- and CO_2-controlled incubation chamber (Zeiss/PeCon) maintained at 37°C and 5% CO_2. Fluorophores were excited using a 561 nm laser with a maximally-sized pinhole, 3.5% laser power, and 800 V detector gain. Movies were acquired with a 40x oil-immersion objective with a numerical aperture of 1.3 using bidirectional scanning to maximize scan speed. Intentional photobleaching (100% 561 nm laser and 100% 405 nm laser) was applied during frame 16.

FRAP analysis

We used custom Python code (https://github.com/vinsfan368/FRAPpy) to quality-control FRAP movies and calculate normalized recoveries. FRAP movies were rejected if there was substantial axial drift.

Fitting FRAP models to experimental data carries model-dependent assumptions (Mueller et al., 2008; Sprague et al., 2004). We followed the analysis scheme outlined by (Mueller et al., 2012), subheading 3.3.2. Briefly, this involves:

1. Defining a nuclear mask for each FRAP movie. We took a sum-intensity projection across the FRAP movie after normalizing each frame by mean-subtraction and dividing by each frame's standard deviation. We applied a Gaussian blur to this image and used isodata thresholding followed by hole-filling to define the nucleus.
2. Background subtracting each frame of the FRAP movie. We took the median value of the pixels of the frame defined as non-nuclear as the "background" of that frame and subtracted this value from all of the pixels in that frame.
3. Normalizing fluorescence values within the nuclear mask to correct for observational photobleaching. Images in the pre-bleach phase of the movie

were normalized such that their nuclear intensities were equal to that of the last frame before photobleaching. Images in the post-bleach phase of the movie were normalized such that their nuclear intensities were equal to that of the first image acquired after bleaching.

4. Calculating FRAP(t), the fluorescence recovery curve over time. At each time point, this was defined as the mean FRAP spot intensity. (These values have been background-subtracted in step 2 and corrected for observational photobleaching in step 3.) We then divided these values by the mean of the pre-bleach frames, which normalizes the FRAP(t) curve to 1.
5. Resampling FRAP(t) using log-spaced bins to prevent overrepresentation of the long FRAP recovery tail. We defined 100 log-spaced bins between 0.01 s and the max time point recorded for any of the movies in a condition. Then, we took the arithmetic mean of both the timestamps and normalized recovery values falling between these bins. These were used to fit recovery curves below.
6. Testing if diffusion plays a role in FRAP recovery with the gradient-smoothing test. We plotted the radial intensity profile of the frames immediately after bleaching, normalized them to between 0 and 1, and checked for shape changes as recovery progressed. We did not see changes that would indicate diffusion is contributing to our measured FRAP recoveries for any condition (Figure 2—figure supplement 4D-F). We also note that for the radius of our bleach spot (0.75 μm) and the diffusion coefficient measured by SMT (slower-diffusing population: ~2 $\mu m^2/s$), we would expect diffusive molecules on the edge of the bleach circle to reach the center in about 70 milliseconds on average (mean squared displacement = 4Dt), and our imaging setup allowed us to capture the first post-bleach frame only ~250 ms after bleaching.
7. Fitting the FRAP(t) curves to a single-exponential recovery function:

$$\mathrm{FRAP}(\Delta t) = A\left(1 - e^{-\Delta t/\tau}\right)$$

with an implicit constant term constraining A to [0, 1]. Only FRAP recovery for H2B-HaloTag was well-fit by this equation. We instead fit FRAP recoveries for the synthetic TFs to a double-exponential recovery function:

$$\mathrm{FRAP}(\Delta t) = A_1\left(1 - e^{-\Delta t/\tau_1}\right) + A_2\left(1 - e^{-\Delta t/\tau_2}\right)$$

also with an implicit constant term constraining A_1 and A_2 to [0, 1] and their sum to [0, 1].

We have tabulated the values from these fits in Supplementary Table 1.

Cleavage under targets and release using nuclease (CUT&RUN) protocol

We followed steps 1-13, 21-37, and 57-60 of a published CUT&RUN protocol (dx.doi.org/10.17504/protocols.io.zcpf2vn), a revised protocol from (Meers et al., 2019), with the following modifications:

Cells were counted prior to mixing with concanavalin A beads, and ~299,000 cells were used for each condition. All cell centrifugation steps were 500 g for three minutes. The digitonin concentration optimized for our U2OS cell lines was 0.02%. For all experimental conditions, we used a polyclonal rabbit anti-V5 antibody (Abcam ab9116). The wash buffer and Dig-wash buffer were supplemented with 1 μM estradiol. All wash steps with the Dig-wash buffer were repeated once (for a total of two washes) with 200 μL of Dig-wash buffer.

Following phenol-chloroform extraction, we used ferromagnetic bead cleanup to concentrate and purify DNA fragments:

1. Add 200 μL SPRI-like homemade magnetic beads to 200 μL eluate from the phenol-chloroform extraction.
2. Add 400 μL of PEG-8000 buffer to this mixture to help precipitate the DNA fragments.
3. Rotate at room temperature for 1 hour.
4. Place the tubes on a magnet stand.
5. Pipette off supernatant.
6. Add 800 μL of freshly-made 80% ethanol to the tube, being careful not to disturb the beads.
7. Pipette off supernatant.
8. Repeat steps 6 and 7.
9. Air-dry the tubes until beads appear dull brown but not dry and cracked.
10. Elute in 21 μL H_2O.

For library preparation, we used NEBNext® Ultra™ II DNA Library Prep Kit for Illumina® and followed the manufacturer's instructions with the following modifications:

The Illumina hairpin adapter was diluted 25-fold (i.e., 1 part concentrated adapter plus 24 parts water). Eleven PCR cycles were used for amplification. We performed a dual-sided bead selection with homemade SPRI-like beads with bead

concentrations 0.67x (and discarding bead-bound large fragments) and 1.0x (and keeping bead-bound fragments). Fragment sizes were checked by Bioanalyzer (Agilent). Libraries were pooled replicate-wise and sequenced on a NextSeq 2000. Two replicates for each condition were sequenced.

Genomics analysis

We generated a custom hg38 genome with our reporter locus engineered at the AAVS1 locus with bespoke bash scripts. We generated bowtie2 indices for this genome and used this as a reference for both ATAC-seq and CUT&RUN data. We also used the blacklist from (Nordin et al., 2023) for both ATAC-seq and CUT&RUN analyses.

We used publicly-available ATAC-seq data (Oomen et al., 2019) in U2OS cells as a baseline for genomic accessibility in our cell line. We used the nf-core (Ewels et al., 2020) pipeline atacseq (Patel et al., 2023) to generate genomic accessibility signal (bigWig files) and to call peaks (BED files). We used the pipeline with following non-default parameters: aligner: 'bowtie2', narrow_peak: true, min_reps_consensus: 2. This dataset had two biological replicates with four technical replicates each; we merged peak sets between the two biological replicates with custom bash scripts for our analyses. For genomic tracks, we took the mean of the two bigWig files corresponding to the two biological replicates.

For our CUT&RUN data, we used the cutandrun (Cheshire et al., 2024) nf-core pipeline with the following non-default parameters: spikein_genome: BDGP6, trim_nextseq: 20, remove_mitochondrial_reads: true, mito_name: chrM, dedup_target_reads: true, use_control: false, seacr_peak_threshold: 0.01, replicate_threshold: 2. This normalized our occupancy data to sheared Drosophila DNA introduced in the CUT&RUN STOP buffer. For genomic tracks and quantification of signal, we took the mean of the two bigWig files corresponding to two biological replicates for each of cell lines expressing synthetic TFs. For peak sets, we limited ourselves to peaks that were reproduced in both replicates. To call CUT&RUN peak overlaps with ATAC-seq peaks (Figure 7—figure supplement 1A), we considered a peak overlapping if at least one basepair of the CUT&RUN peak was shared with any ATAC-seq peak.

Acknowledgements

A heartfelt thank you to all members of the Tjian+Darzacq and Staller groups for their intellectual input and experimental advice for this project, particularly Djem Kissiov, Claudia Cattoglio, Joseph McKenna, Yu Chen, Aditya Udupa, Oscar Whitney, and Alec Heckert. Thank you to Anna Mapp for suggesting the norstictic acid experiment. A large thanks to Sathvik Anantakrishnan for his efforts on microscope automation and maintenance, without which this project would not have been possible. We thank Djem Kissiov, Aditya Udupa, and Robert Tjian for the careful reading of the manuscript. We thank Anders Näär and Haribabu Arthanari for helpful discussions. We thank Luke Lavis for providing us with Janelia Fluor dyes. We thank James McNally for helpful correspondence and code sharing. We thank the Dillin lab, particularly Kimberly Tsui, for training and use of the Incucyte S3 instrument.

Author contributions

V.B.F. and M.V.S. conceptualized the study. V.B.F. executed experiments and performed analysis. A.A.A. and T.G.W.G. guided the design of the PAPA experiments, and A.A.A. advised on the setup and analysis of the PAPA experiments. M.V.S. and X.D. supervised the project. V.B.F. and M.V.S. wrote the manuscript. T.G.W.G revised the manuscript. X.D. and M.V.S. acquired funding for the project.

Funding

M.V.S. is supported by Simons Foundation grant 1018719, NSF grant 2112057, and NIH grant R35GM150813. M.V.S. is a Chan Zuckerberg Biohub – San Francisco Investigator. A.A.A. was supported by the Howard Hughes Medical Institute. T.G.W.G. was supported by NIH grant 1RM1GM139738. Funding to X.D. was provided by the Silicon Valley Community Foundation/CZI (RR-8175).

Competing interests

X.D. is a co-founder of Eikon Therapeutics, Inc. All other authors state they have no competing interests.

Materials availability

Plasmids used in this study have been deposited with Addgene (Addgene ID numbers 240165-240174). Cell lines are available upon reasonable request.

Data availability

SMT trajectories (CSV files tabulating all detections surviving filtering steps) are available on Dryad (https://doi.org/10.5061/dryad.41ns1rnqt). We were unable to deposit underlying SMT movies due to their large size. FRAP movies are also available as part of the same Dryad dataset (https://doi.org/10.5061/dryad.41ns1rnqt).

CUT&RUN data has been deposited to the Sequence Read Archive and is available as PRJNA1305492. ATAC-seq data from (Oomen et al., 2019) is available on the GEO as Series GSE121840.

Code availability

All essential code is available on public GitHub repositories. We used quot to detect, localize, and connect spots in SMT movies; commit 1b9051e of https://github.com/vinsfan368/quot was used for this article (a fork of https://github.com/alecheckert/quot). We used qtpicker to refine nuclear masks; commit 6bcbf12 of https://github.com/vinsfan368/qtpicker was used for this article. We used saspt (Heckert et al., 2022) to generate posterior diffusion spectra; commit 632faad of https://github.com/vinsfan368/saspt was used for this article (a fork of https://github.com/alecheckert/saspt). We used FRAPpy to analyze FRAP movies from CZI files; commit dc3687d of https://github.com/vinsfan368/FRAPpy was used for this article.

All other code is available upon reasonable request.

References

Abidi AA, Dailey GM, Tjian R, Graham TGW. 2025. Collective unstructured interactions drive chromatin binding of transcription factors. *bioRxivorg*. doi:10.1101/2025.05.16.654615

Alberts B, Johnson A, Lewis J, Raff M, Roberts K, Walter P. 2002. Molecular Biology of the Cell. *Garland Science*. https://www.ncbi.nlm.nih.gov/books/NBK21054/

Alerasool N, Leng H, Lin Z-Y, Gingras A-C, Taipale M. 2022. Identification and functional characterization of transcriptional activators in human cells. *Mol Cell* **82**:677–695.e7.

Badis G, Berger MF, Philippakis AA, Talukder S, Gehrke AR, Jaeger SA, Chan ET, Metzler G, Vedenko A, Chen X, Kuznetsov H, Wang C-F, Coburn D, Newburger DE, Morris Q, Hughes TR, Bulyk ML. 06 2009. Diversity and complexity in DNA recognition by transcription factors. *Science* **324**:1720–1723.

Barrera LA, Vedenko A, Kurland JV, Rogers JM, Gisselbrecht SS, Rossin EJ, Woodard J, Mariani L, Kock KH, Inukai S, Siggers T, Shokri L, Gordân R, Sahni N, Cotsapas C, Hao T, Yi S, Kellis M, Daly MJ, Vidal M, Hill DE, Bulyk ML. 2016. Survey of variation in human transcription factors reveals prevalent DNA binding changes. *Science* **351**:1450–1454.

Baughman HER, Narang D, Chen W, Villagrán Suárez AC, Lee J, Bachochin MJ, Gunther TR, Wolynes PG, Komives EA. 2022. An intrinsically disordered transcription activation domain increases the DNA binding affinity and reduces the specificity of NFκB p50/RelA. *Journal of Biological Chemistry*. doi:10.1016/j.jbc.2022.102349

Bentley EP, Scholl D, Wright PE, Deniz AA. 2023. Coupling of binding and differential subdomain folding of the intrinsically disordered transcription factor CREB. *FEBS Lett* **597**:917–932.

Berlow RB, Dyson HJ, Wright PE. 2017. Hypersensitive termination of the hypoxic response by a disordered protein switch. *Nature* **543**:447–451.

Bjarnason S, McIvor J, Prestel A, Demeny K, Bullerjahn J, Kragelund BB, Mercadante D, Heidarsson PO. 2024. DNA binding redistributes activation domain ensemble and accessibility in pioneer factor Sox2. *Biophys J* **123**:73a.

Brent R, Ptashne M. 1985. A eukaryotic transcriptional activator bearing the DNA specificity of a prokaryotic repressor. *Cell* **43**:729–736.

Brodaczewska KK, Szczylik C, Fiedorowicz M, Porta C, Czarnecka AM. 2016. Choosing the right cell line for renal cell cancer research. *Mol Cancer* **15**. doi:10.1186/s12943-016-0565-8

Brodsky S, Jana T, Mittelman K, Chapal M, Kumar DK, Carmi M, Barkai N. 2020. Intrinsically Disordered Regions Direct Transcription Factor In Vivo Binding Specificity. *Mol Cell* **79**:459–471.e4.

Brouwer I, Lenstra TL. 2019. Visualizing transcription: key to understanding gene expression dynamics. *Curr Opin Chem Biol* **51**:122–129.

Callegari A, Sieben C, Benke A, Suter DM, Fierz B, Mazza D, Manley S. 01 2019. Single-molecule dynamics and genome-wide transcriptomics reveal that NF-kB (p65)-DNA binding times can be decoupled from transcriptional activation. *PLoS Genet* **15**:e1007891– 23.

Chen J, Zhang Z, Li L, Chen B-C, Revyakin A, Hajj B, Legant W, Dahan M, Lionnet T, Betzig E, Tjian R, Liu Z. 2014. Single-molecule dynamics of enhanceosome assembly in embryonic stem cells. *Cell* **156**:1274–1285.

Chen Y, Cattoglio C, Dailey GM, Zhu Q, Tjian R, Darzacq X. 2022. Mechanisms governing target search and binding dynamics of hypoxia-inducible factors. *Elife* **11**. doi:10.7554/eLife.75064

Cheshire C, charlotte-west, Rönkkö T, Bot N-C, Patel H, tamara-hodgetts, Ladd D, Thiery A, Fields C, Deu-Pons J, Ewels P, Möller S, Menden K. 2024. nf-core/cutandrun: nf-core/cutandrun v3.2.2 Iridium Ibis. Zenodo. doi:10.5281/ZENODO.10606804

Cho W-K, Spille J-H, Hecht M, Lee C, Li C, Grube V, Cisse II. 07 2018. Mediator and RNA polymerase II clusters associate in transcription-dependent condensates. *Science* **361**:412–415.

Copeland JW, Nasiadka A, Dietrich BH, Krause HM. 1996. Patterning of the Drosophila embryo by a homeodomain-deleted Ftz polypeptide. *Nature* **379**:162–165.

Cowling VH, Cole MD. 2007. The Myc transactivation domain promotes global phosphorylation of the

RNA polymerase II carboxy-terminal domain independently of direct DNA binding. *Mol Cell Biol* **27**:2059–2073.
Craig N, Green R, Greider C, Storz G, Wolberger C. 2021. Molecular biology: Principles of genome function, 3rd ed. London, England: Oxford University Press.
Cress WD, Triezenberg SJ. 01 1991. Critical structural elements of the VP16 transcriptional activation domain. *Science* **251**:87–90.
Crocker J, Abe N, Rinaldi L, McGregor AP, Frankel N, Wang S, Alsawadi A, Valenti P, Plaza S, Payre F, Mann RS, Stern DL. 2015. Low affinity binding site clusters confer hox specificity and regulatory robustness. *Cell* **160**:191–203.
Currie SL, Lau DKW, Doane JJ, Whitby FG, Okon M, McIntosh LP, Graves BJ. 2017. Structured and disordered regions cooperatively mediate DNA-binding autoinhibition of ETS factors ETV1, ETV4 and ETV5. *Nucleic Acids Res* **45**:2223–2241.
Dahal L, Graham TGW, Dailey GM, Heckert A, Tjian R, Darzacq X. 2025. Surprising features of nuclear receptor interaction networks revealed by live-cell single-molecule imaging. *Elife* **12**. doi:10.7554/eLife.92979
Danner E. 2020. Effective Lonza 4D Nucleofection with Inexpensive Homemade Buffers. *protocols.io*. https://www.protocols.io/view/effective-lonza-4d-nucleofection-with-inexpensive-64mhgu6
De Guzman RN, Martinez-Yamout MA, Dyson HJ, Wright PE. 2004. Interaction of the TAZ1 domain of the CREB-binding protein with the activation domain of CITED2: regulation by competition between intrinsically unstructured ligands for non-identical binding sites. *J Biol Chem* **279**:3042–3049.
DelRosso N, Suzuki PH, Griffith D, Lotthammer JM, Novak B, Kocalar S, Sheth MU, Holehouse AS, Bintu L, Fordyce P. 2024. High-throughput affinity measurements of direct interactions between activation domains and co-activators. *bioRxivorg* 2024.08.19.608698.
DelRosso N, Tycko J, Suzuki P, Andrews C, Aradhana, Mukund A, Liongson I, Ludwig C, Spees K, Fordyce P, Bassik MC, Bintu L. 2023. Large-scale mapping and mutagenesis of human transcriptional effector domains. *Nature* 1–8.
Doughty BR, Hinks MM, Schaepe JM, Marinov GK, Thurm AR, Rios-Martinez C, Parks BE, Tan Y, Marklund E, Dubocanin D, Bintu L, Greenleaf WJ. 2024. Single-molecule states link transcription factor binding to gene expression. *Nature* **636**:745–754.
Driouchi A, Bretan M, Davis BJ, Heckert A, Seeger M, Silva MB, Forrest WSR, Hsiung J, Tan J, Yang H, McSwiggen DT, Song L, Sule A, Abaie B, Chen H, Chhun B, Conroy B, Elliott LA, Gonzalez E, Ilkov F, Isaacs J, Labaria G, Lagana M, Larsen DD, Margolin B, Nguyen MK, Park E, Rine J, Tang Y, Vana M, Wilkey A, Zhang Z, Basham S, Ho JJ, Johnson S, Klammer AA, Lin K, Darzacq X, Betzig E, Berman RT, Anderson DJ. 2025. Oblique line scan illumination enables expansive, accurate and sensitive single-protein measurements in solution and in living cells. *Nat Methods* **22**:559–568.
Dubnau J, Struhl G. 1996. RNA recognition and translational regulation by a homeodomain protein. *Nature* **379**:694–699.
Dyson HJ, Wright PE. 2016. Role of Intrinsic Protein Disorder in the Function and Interactions of the Transcriptional Coactivators CREB-binding Protein (CBP) and p300. *J Biol Chem* **291**:6714–6722.
El-Gebali S, Mistry J, Bateman A, Eddy SR, Luciani A, Potter SC, Qureshi M, Richardson LJ, Salazar GA, Smart A, Sonnhammer ELL, Hirsh L, Paladin L, Piovesan D, Tosatto SCE, Finn RD. 2019. The Pfam protein families database in 2019. *Nucleic Acids Res* **47**:D427–D432.
Endesfelder U, Heilemann M. 2015. Direct stochastic optical reconstruction microscopy (dSTORM). *Methods Mol Biol* **1251**:263–276.
Erijman A, Kozlowski L, Sohrabi-Jahromi S, Fishburn J, Warfield L, Schreiber J, Noble WS, Söding J, Hahn S. 2020. A High-Throughput Screen for Transcription Activation Domains Reveals Their Sequence Features and Permits Prediction by Deep Learning. *Mol Cell* **78**:890–902.e6.
Ewels PA, Peltzer A, Fillinger S, Patel H, Alneberg J, Wilm A, Garcia MU, Di Tommaso P, Nahnsen S. 2020. The nf-core framework for community-curated bioinformatics pipelines. *Nat Biotechnol* **38**:276–278.
Fallacaro S, Mukherjee A, Ratchasanmuang P, Zinski J, Haloush YI, Shankta K, Mir M. 2024. A fine

kinetic balance of interactions directs transcription factor hubs to genes. *Molecular Biology*.
Ferrie JJ, Karr JP, Graham TGW, Dailey GM, Zhang G, Tjian R, Darzacq X. 2024. P300 is an obligate integrator of combinatorial transcription factor inputs. *Mol Cell* **84**:234–243.e4.
Ferrie JJ, Karr JP, Tjian R, Darzacq X. 2022. "Structure"-function relationships in eukaryotic transcription factors: The role of intrinsically disordered regions in gene regulation. *Mol Cell* **82**:3970–3984.
Finn RD, Coggill P, Eberhardt RY, Eddy SR, Mistry J, Mitchell AL, Potter SC, Punta M, Qureshi M, Sangrador-Vegas A, Salazar GA, Tate J, Bateman A. 2016. The Pfam protein families database: towards a more sustainable future. *Nucleic Acids Res* **44**:D279–85.
Garlick JM, Sturlis SM, Bruno PA, Yates JA, Peiffer AL, Liu Y, Goo L, Bao L, De Salle SN, Tamayo-Castillo G, Brooks CL 3rd, Merajver SD, Mapp AK. 2021. Norstictic acid is a selective allosteric transcriptional regulator. *J Am Chem Soc* **143**:9297–9302.
Gera T, Jonas F, More R, Barkai N. 2022. Evolution of binding preferences among whole-genome duplicated transcription factors. *Elife* **11**:e73225.
Gillespie MA, Palii CG, Sanchez-Taltavull D, Shannon P, Longabaugh WJR, Downes DJ, Sivaraman K, Espinoza HM, Hughes JR, Price ND, Perkins TJ, Ranish JA, Brand M. 2020. Absolute quantification of transcription factors reveals principles of gene regulation in erythropoiesis. *Mol Cell* **78**:960–974.e11.
Gill G, Pascal E, Tseng ZH, Tjian R. 1994. A glutamine-rich hydrophobic patch in transcription factor Sp1 contacts the dTAFII110 component of the Drosophila TFIID complex and mediates transcriptional activation. *Proceedings of the National Academy of Sciences* **91**:192–196.
Goldman N, Chandra A, Johnson I, Sullivan MA, Patil AR, Vanderbeck A, Jay A, Zhou Y, Ferrari EK, Mayne L, Aguilan J, Xue H-H, Faryabi RB, John Wherry E, Sidoli S, Maillard I, Vahedi G. 2023. Intrinsically disordered domain of transcription factor TCF-1 is required for T cell developmental fidelity. *Nat Immunol*. doi:10.1038/s41590-023-01599-7
Golemis EA, Brent R. 1992. Fused protein domains inhibit DNA binding by LexA. *Mol Cell Biol* **12**:3006–3014.
Graham TGW, Dugast-Darzacq C, Dailey GM, Weng B, Anantakrishnan S, Darzacq X, Tjian R. 2025. Single-molecule live imaging of subunit interactions and exchange within cellular regulatory complexes. *Mol Cell* **85**:2854–2868.e7.
Graham TGW, Ferrie JJ, Dailey GM, Tjian R, Darzacq X. 2022. Detecting molecular interactions in live-cell single-molecule imaging with proximity-assisted photoactivation (PAPA). *Elife* **11**. doi:10.7554/eLife.76870
Grimm JB, Xie L, Casler JC, Patel R, Tkachuk AN, Falco N, Choi H, Lippincott-Schwartz J, Brown TA, Glick BS, Liu Z, Lavis LD. 2021. A general method to improve fluorophores using deuterated auxochromes. *JACS Au* **1**:690–696.
Guo M, Song L-P, Jiang Y, Liu W, Yu Y, Chen G-Q. 2006. Hypoxia-mimetic agents desferrioxamine and cobalt chloride induce leukemic cell apoptosis through different hypoxia-inducible factor-1alpha independent mechanisms. *Apoptosis* **11**:67–77.
Hahn S, Young ET. 2011. Transcriptional regulation in Saccharomyces cerevisiae: transcription factor regulation and function, mechanisms of initiation, and roles of activators and coactivators. *Genetics* **189**:705–736.
Hansen AS, Woringer M, Grimm JB, Lavis LD, Tjian R, Darzacq X. 2018. Robust model-based analysis of single-particle tracking experiments with Spot-On. *Elife* **7**. doi:10.7554/eLife.33125
Harrison MM, Li X-Y, Kaplan T, Botchan MR, Eisen MB. 2011. Zelda binding in the early Drosophila melanogaster embryo marks regions subsequently activated at the maternal-to-zygotic transition. *PLoS Genet* **7**:e1002266.
Heckert A, Dahal L, Tijan R, Darzacq X. 2022. Recovering mixtures of fast-diffusing states from short single-particle trajectories. *Elife* **11**. doi:10.7554/eLife.70169
He F, Borcherds W, Song T, Wei X, Das M, Chen L, Daughdrill GW, Chen J. 2019. Interaction between p53 N terminus and core domain regulates specific and nonspecific DNA binding. *Proceedings of the National Academy of Sciences* **116**:8859–8868.

Henderson AR, Henley MJ, Foster NJ, Peiffer AL, Beyersdorf MS, Stanford KD, Sturlis SM, Linhares BM, Hill ZB, Wells JA, Cierpicki T, Brooks CL, Fierke CA, Mapp AK. 09 2018. Conservation of coactivator engagement mechanism enables small-molecule allosteric modulators. *Proceedings of the National Academy of Sciences* **115**:8960–8965.

Henley MJ, Linhares BM, Morgan BS, Cierpicki T, Fierke CA, Mapp AK. 2020. Unexpected specificity within dynamic transcriptional protein–protein complexes. *Proceedings of the National Academy of Sciences* **117**:27346–27353.

Hewitson KS, McNeill LA, Riordan MV, Tian Y-M, Bullock AN, Welford RW, Elkins JM, Oldham NJ, Bhattacharya S, Gleadle JM, Ratcliffe PJ, Pugh CW, Schofield CJ. 2002. Hypoxia-inducible factor (HIF) asparagine hydroxylase is identical to factor inhibiting HIF (FIH) and is related to the cupin structural family. *J Biol Chem* **277**:26351–26355.

Hope IA, Mahadevan S, Struhl K. 1988. Structural and functional characterization of the short acidic transcriptional activation region of yeast GCN4 protein. *Nature* **333**:635–640.

Hope IA, Struhl K. 1986. Functional dissection of a eukaryotic transcriptional activator protein, GCN4 of yeast. *Cell* **46**:885–894.

Hume MA, Barrera LA, Gisselbrecht SS, Bulyk ML. 2015. UniPROBE, update 2015: new tools and content for the online database of protein-binding microarray data on protein-DNA interactions. *Nucleic Acids Res* **43**:D117–22.

Hurieva B, Kumar DK, Morag R, Lupo O, Carmi M, Barkai N, Jonas F. 2024. Disordered sequences of transcription factors regulate genomic binding by integrating diverse sequence grammars and interaction types. *Nucleic Acids Res* **52**:8763–8777.

Jana T, Brodsky S, Barkai N. 2021. Speed–Specificity Trade-Offs in the Transcription Factors Search for Their Genomic Binding Sites. *Trends Genet* **37**:421–432.

Jeon J, Friedman LJ, Zhou DH, Seo HD, Adeleke OA, Graham B, Patteson EF, Gelles J, Buratowski S. 2025. Single-molecule analysis of transcription activation: dynamics of SAGA coactivator recruitment. *Nat Struct Mol Biol* **32**:675–686.

Jolma A, Yan J, Whitington T, Toivonen J, Nitta KR, Rastas P, Morgunova E, Enge M, Taipale M, Wei G, Palin K, Vaquerizas JM, Vincentelli R, Luscombe NM, Hughes TR, Lemaire P, Ukkonen E, Kivioja T, Taipale J. 2013. DNA-binding specificities of human transcription factors. *Cell* **152**:327–339.

Jonas F, Carmi M, Krupkin B, Steinberger J, Brodsky S, Jana T, Barkai N. 2023. The molecular grammar of protein disorder guiding genome-binding locations. *Nucleic Acids Res*. doi:10.1093/nar/gkad184

Kadoch C, Crabtree GR. 2015. Mammalian SWI/SNF chromatin remodeling complexes and cancer: Mechanistic insights gained from human genomics. *Science advances* **1**:e1500447–e1500447.

Kawasaki K, Fukaya T. 2023. Functional coordination between transcription factor clustering and gene activity. *Mol Cell* **83**:1605–1622.e9.

Keegan L, Gill G, Ptashne M. 1986. Separation of DNA binding from the transcription-activating function of a eukaryotic regulatory protein. *Science* **231**:699–704.

Krois AS, Dyson HJ, Wright PE. 2018. Long-range regulation of p53 DNA binding by its intrinsically disordered N-terminal transactivation domain. *Proceedings of the National Academy of Sciences* **115**:E11302–E11310.

Kühn S, Nasufovic V, Wilhelm J, Kompa J, de Lange EMF, Lin Y-H, Egoldt C, Fischer J, Lennoi A, Tarnawski M, Reinstein J, Vlijm R, Hiblot J, Johnsson K. 2025. SNAP-tag2 for faster and brighter protein labeling. *Nat Chem Biol* 1–8.

Kumar DK, Jonas F, Jana T, Brodsky S, Carmi M, Barkai N. 2023. Complementary strategies for directing in vivo transcription factor binding through DNA binding domains and intrinsically disordered regions. *Mol Cell* **0**. doi:10.1016/j.molcel.2023.04.002

Kvon EZ, Stampfel G, Yáñez-Cuna JO, Dickson BJ, Stark A. 2012. HOT regions function as patterned developmental enhancers and have a distinct cis-regulatory signature. *Genes Dev* **26**:908–913.

Lando D, Peet DJ, Gorman JJ, Whelan DA, Whitelaw ML, Bruick RK. 2002a. FIH-1 is an asparaginyl hydroxylase enzyme that regulates the transcriptional activity of hypoxia-inducible factor. *Genes Dev* **16**:1466–1471.

Lando D, Peet DJ, Whelan DA, Gorman JJ, Whitelaw ML. 2002b. Asparagine hydroxylation of the HIF transactivation domain a hypoxic switch. *Science* **295**:858–861.
Lasko LM, Jakob CG, Edalji RP, Qiu W, Montgomery D, Digiammarino EL, Hansen TM, Risi RM, Frey R, Manaves V, Shaw B, Algire M, Hessler P, Lam LT, Uziel T, Faivre E, Ferguson D, Buchanan FG, Martin RL, Torrent M, Chiang GG, Karukurichi K, Langston JW, Weinert BT, Choudhary C, de Vries P, Van Drie JH, McElligott D, Kesicki E, Marmorstein R, Sun C, Cole PA, Rosenberg SH, Michaelides MR, Lai A, Bromberg KD. 2017. Discovery of a selective catalytic p300/CBP inhibitor that targets lineage-specific tumours. *Nature* **550**:128–132.
Latchman DS. 2008. Eukaryotic Transcription Factors, 5th Edition. ed. Elsevier Science.
Lauberth SM, Nakayama T, Wu X, Ferris AL, Tang Z, Hughes SH, Roeder RG. 02 2013. H3K4me3 interactions with TAF3 regulate preinitiation complex assembly and selective gene activation. *Cell* **152**:1021– 1036.
Li J, White JT, Saavedra H, Wrabl JO, Motlagh HN, Liu K, Sowers J, Schroer T, Thompson EB, Hilser VJ. 10 2017. Genetically tunable frustration controls allostery in an intrinsically disordered transcription factor. *Elife* **6**:e30688.
Lionnet T, Wu C. 2021. Single-molecule tracking of transcription protein dynamics in living cells: seeing is believing, but what are we seeing? *Curr Opin Genet Dev* **67**:94–102.
Liu J, Perumal NB, Oldfield CJ, Su EW, Uversky VN, Dunker AK. 06 2006. Intrinsic disorder in transcription factors. *Biochemistry* **45**:6873–6888.
Liu Y, Matthews KS, Bondos SE. 2008. Multiple intrinsically disordered sequences alter DNA binding by the homeodomain of the Drosophila hox protein ultrabithorax. *J Biol Chem* **283**:20874–20887.
Liu Z, Legant WR, Chen B-C, Li L, Grimm JB, Lavis LD, Betzig E, Tjian R. 2014. 3D imaging of Sox2 enhancer clusters in embryonic stem cells. *Elife* **3**:e04236.
Lum JK, Majmudar CY, Ansari AZ, Mapp AK. 2006. Converting inactive peptides into potent transcriptional activators. *ACS Chem Biol* **1**:639–643.
Lu Z, Rowe SP, Brennan BB, Davis SE, Metzler RE, Nau JJ, Majmudar CY, Mapp AK, Ansari AZ. 2005. Unraveling the mechanism of a potent transcriptional activator. *J Biol Chem* **280**:29689–29698.
Mahendrawada L, Warfield L, Donczew R, Hahn S. 2025. Low overlap of transcription factor DNA binding and regulatory targets. *Nature* 1–9.
Ma J, Ptashne M. 10 1987. A new class of yeast transcriptional activators. *Cell* **51**:113–119.
Malik S, Roeder RG. 2010. The metazoan Mediator co-activator complex as an integrative hub for transcriptional regulation. *Nat Rev Genet* **11**:761–772.
Már M, Nitsenko K, Heidarsson PO. 2023. Multifunctional Intrinsically Disordered Regions in Transcription Factors. *Chemistry* e202203369.
Mazzocca M, Loffreda A, Colombo E, Fillot T, Gnani D, Falletta P, Monteleone E, Capozi S, Bertrand E, Legube G, Lavagnino Z, Tacchetti C, Mazza D. 2023. Chromatin organization drives the search mechanism of nuclear factors. *Nat Commun* **14**:6433.
Meers MP, Bryson TD, Henikoff JG, Henikoff S. 2019. Improved CUT&RUN chromatin profiling tools. *Elife* **8**:e46314.
Mindel V, Brodsky S, Cohen A, Manadre W, Jonas F, Carmi M, Barkai N. 2024a. Intrinsically disordered regions of the Msn2 transcription factor encode multiple functions using interwoven sequence grammars. *Nucleic Acids Res* **52**:2260–2272.
Mindel V, Brodsky S, Yung H, Manadre W, Barkai N. 2024b. Revisiting the model for coactivator recruitment: Med15 can select its target sites independent of promoter-bound transcription factors. *Nucleic Acids Res* **52**:12093–12111.
Morffy N, Van den Broeck L, Miller C, Emenecker RJ, Bryant JA Jr, Lee TM, Sageman-Furnas K, Wilkinson EG, Pathak S, Kotha SR, Lam A, Mahatma S, Pande V, Waoo A, Wright RC, Holehouse AS, Staller MV, Sozzani R, Strader LC. 2024. Identification of plant transcriptional activation domains. *Nature* **632**:166–173.
Mueller F, Karpova TS, Mazza D, McNally JG. 2012. Monitoring dynamic binding of chromatin proteins in vivo by fluorescence recovery after photobleaching. *Methods Mol Biol* **833**:153–176.

Mueller F, Wach P, McNally JG. 2008. Evidence for a common mode of transcription factor interaction with chromatin as revealed by improved quantitative fluorescence recovery after photobleaching. *Biophys J* **94**:3323–3339.
Ning S, Chao H-J, Li S, Zhou R, Zou L, Zhang X, Liu J, Yan D, Duan M. 2022. The auto-inhibition mechanism of transcription factor Ets-1 induced by phosphorylation on the intrinsically disordered region. *Comput Struct Biotechnol J* **20**:1132–1141.
Nordin A, Zambanini G, Pagella P, Cantù C. 2023. The CUT&RUN suspect list of problematic regions of the genome. *Genome Biol* **24**:185.
Noyes MB, Meng X, Wakabayashi A, Sinha S, Brodsky MH, Wolfe SA. 2008. A systematic characterization of factors that regulate Drosophila segmentation via a bacterial one-hybrid system. *Nucleic Acids Res* **36**:2547–2560.
Oomen ME, Hansen AS, Liu Y, Darzacq X, Dekker J. 2019. CTCF sites display cell cycle-dependent dynamics in factor binding and nucleosome positioning. *Genome Res* **29**:236–249.
Park M, Patel N, Keung AJ, Khalil AS. 2019. Engineering Epigenetic Regulation Using Synthetic Read-Write Modules. *Cell* **176**:227–238.e20.
Patel H, Espinosa-Carrasco J, Langer B, Ewels P, Bot N-C, Garcia MU, Syme R, Peltzer A, Talbot A, Behrens D, Gabernet G, Jin M, Hörtenhuber M, Rodriguez JG, Menden K, An Ö. 2023. nf-core/atacseq: [2.1.2] - 2022-08-07. Zenodo. doi:10.5281/ZENODO.8222875
Ptashne M. 1988. How eukaryotic transcriptional activators work. *Nature* **335**:683–689.
Ptashne M, Gann A. 04 1997. Transcriptional activation by recruitment. *Nature* **386**:569– 577.
Pufall MA, Lee GM, Nelson ML, Kang H-S, Velyvis A, Kay LE, McIntosh LP, Graves BJ. 2005. Variable Control of Ets-1 DNA Binding by Multiple Phosphates in an Unstructured Region. *Science* **309**:142–145.
Riley TR, Slattery M, Abe N, Rastogi C, Liu D, Mann RS, Bussemaker HJ. 2014. SELEX-seq: a method for characterizing the complete repertoire of binding site preferences for transcription factor complexes. *Methods Mol Biol* **1196**:255–278.
Sadowski I, Ma J, Triezenberg S, Ptashne M. 10 1988. GAL4-VP16 is an unusually potent transcriptional activator. *Nature* **335**:563–564.
Sanborn AL, Yeh BT, Feigerle JT, Hao CV, Townshend RJL, Lieberman-Aiden E, Dror RO, Kornberg RD. 2021. Simple biochemical features underlie transcriptional activation domain diversity and dynamic, fuzzy binding to Mediator. *Elife* **10**:e68068.
Schaepe JM, Fries T, Doughty BR, Crocker OJ, Hinks MM, Marklund E, Greenleaf WJ. 2025. Thermodynamic principles link in vitro transcription factor affinities to single-molecule chromatin states in cells. *bioRxiv*. doi:10.1101/2025.01.27.635162
Schick S, Grosche S, Kohl KE, Drpic D, Jaeger MG, Marella NC, Imrichova H, Lin J-MG, Hofstätter G, Schuster M, Rendeiro AF, Koren A, Petronczki M, Bock C, Müller AC, Winter GE, Kubicek S. 2021. Acute BAF perturbation causes immediate changes in chromatin accessibility. *Nat Genet* **53**:269–278.
Schmidt U, Weigert M, Broaddus C, Myers G. 2018. Cell detection with star-convex polygonsMedical Image Computing and Computer Assisted Intervention – MICCAI 2018, Lecture Notes in Computer Science. Cham: Springer International Publishing. pp. 265–273.
Sigler PB. 05 1988. Transcriptional activation. Acid blobs and negative noodles. *Nature* **333**:210–212.
Skene PJ, Henikoff S. 2017. An efficient targeted nuclease strategy for high-resolution mapping of DNA binding sites. *Elife* **6**:e21856.
Soto LF, Li Z, Santoso CS, Berenson A, Ho I, Shen VX, Yuan S, Bass JIF. 2021. Compendium of human transcription factor effector domains. *Molecular Cell* **82**:514–526.
Spitz F, Furlong EEM. 2012. Transcription factors: from enhancer binding to developmental control. *Nat Rev Genet* **13**:613–626.
Sprague BL, Pego RL, Stavreva DA, McNally JG. 2004. Analysis of binding reactions by fluorescence recovery after photobleaching. *Biophys J* **86**:3473–3495.
Staller MV. 2022. Transcription factors perform a 2-step search of the nucleus. *Genetics* **222**.

doi:10.1093/genetics/iyac111
Staller MV, Holehouse AS, Swain-Lenz D, Das RK, Pappu RV, Cohen BA. 2018. A high-throughput mutational scan of an intrinsically disordered acidic transcriptional activation domain. *Cell Syst* **6**:444–455.e6.
Staller MV, Ramirez E, Kotha SR, Holehouse AS, Pappu RV, Cohen BA. 2022. Directed mutational scanning reveals a balance between acidic and hydrophobic residues in strong human activation domains. *Cell Systems* **13**:334–345.e5.
Stormo GD. 2013. Introduction to protein-DNA interactions: structure, thermodynamics, and bioinformatics. Cold Spring Harbor Laboratory Press.
Stringer C, Wang T, Michaelos M, Pachitariu M. 2021. Cellpose: a generalist algorithm for cellular segmentation. *Nat Methods* **18**:100–106.
Strugo N, Burstein C, Hossain SS, Nago N, Khamis H, Kaplan A. 2025. Intrinsically disordered regions facilitate Msn2 target search to drive promoter selectivity. *bioRxiv*. doi:10.1101/2025.05.23.654710
Struhl K. 1993. Yeast transcription factors. *Curr Opin Cell Biol* **5**:513–520.
Struhl K. 1989. Molecular mechanisms of transcriptional regulation in yeast. *Annu Rev Biochem* **58**:1051–1077.
Struhl K. 1987. Promoters, activator proteins, and the mechanism of transcriptional initiation in yeast. *Cell* **49**:295–297.
Sun X, Dyson HJ, Wright PE. 2021. A phosphorylation-dependent switch in the disordered p53 transactivation domain regulates DNA binding. *Proc Natl Acad Sci U S A* **118**. doi:10.1073/pnas.2021456118
Tang Z, Chen W-Y, Shimada M, Nguyen UTT, Kim J, Sun X-J, Sengoku T, McGinty RK, Fernandez JP, Muir TW, Roeder RG. 07 2013. SET1 and p300 act synergistically, through coupled histone modifications, in transcriptional activation by p53. *Cell* **154**:297– 310.
Teytelman L, Thurtle DM, Rine J, van Oudenaarden A. 2013. Highly expressed loci are vulnerable to misleading ChIP localization of multiple unrelated proteins. *Proceedings of the National Academy of Sciences* **110**:18602–18607.
Tokunaga M, Imamoto N, Sakata-Sogawa K. 2008. Highly inclined thin illumination enables clear single-molecule imaging in cells. *Nat Methods* **5**:159–161.
Trojanowski J, Frank L, Rademacher A, Mücke N, Grigaitis P, Rippe K. 2022. Transcription activation is enhanced by multivalent interactions independent of phase separation. *Mol Cell* **82**:1878–1893.e10.
Udupa A, Kotha SR, Staller MV. 2024. Commonly asked questions about transcriptional activation domains. *Curr Opin Struct Biol* **84**:102732.
Verma M, Choi J, Cottrell KA, Lavagnino Z, Thomas EN, Pavlovic-Djuranovic S, Szczesny P, Piston DW, Zaher HS, Puglisi JD, Djuranovic S. 2019. A short translational ramp determines the efficiency of protein synthesis. *Nat Commun* **10**:5774.
Walther N, Anantakrishnan S, Graham TGW, Dailey GM, Tjian R, Darzacq X. 2024. Automated live-cell single-molecule tracking in enteroid monolayers reveals transcription factor dynamics probing lineage-determining function. *Cell Rep* **43**:114914.
Whitney PH, Lionnet T. 2024. The method in the madness: Transcriptional control from stochastic action at the single-molecule scale. *Curr Opin Struct Biol* **87**:102873.
Xiang L, Chen K, Yan R, Li W, Xu K. 2020. Single-molecule displacement mapping unveils nanoscale heterogeneities in intracellular diffusivity. *Nat Methods* **17**:524–530.
Zhang Z, English BP, Grimm JB, Kazane SA, Hu W, Tsai A, Inouye C, You C, Piehler J, Schultz PG, Lavis LD, Revyakin A, Tjian R. 09 2016. Rapid dynamics of general transcription factor TFIIB binding during preinitiation complex assembly revealed by single-molecule analysis. *Genes Dev* **30**:2106–2118.
Zhou DH, Jeon J, Farheen N, Friedman LJ, Kondev J, Buratowski S, Gelles J. 2024. Mechanisms of synergistic Mediator recruitment in RNA polymerase II transcription activation revealed by single-molecule fluorescence. *bioRxivorg*. doi:10.1101/2024.12.10.627625
Zhu F, Farnung L, Kaasinen E, Sahu B, Yin Y, Wei B, Dodonova S, Nitta K, Morgunova E, Taipale M,

Cramer P, Taipale J. 2017. The interaction landscape between transcription factors and the nucleosome. *Nature* **562**:76–81.